Science Advances
AAAS

advances.sciencemag.org/cgi/content/full/5/8/eaaw7757/DC1

# Supplementary Materials for

## Tuning conformation, assembly, and charge transport properties of conjugated polymers by printing flow

Kyung Sun Park, Justin J. Kwok, Rishat Dilmurat, Ge Qu, Prapti Kafle, Xuyi Luo, Seok-Heon Jung, Yoann Olivier, Jin-Kyun Lee, Jianguo Mei, David Beljonne, Ying Diao*

*Corresponding author. Email: yingdiao@illinois.edu

Published 9 August 2019, *Sci. Adv.* **5**, eaaw7757 (2019)
DOI: 10.1126/sciadv.aaw7757

**The PDF file includes:**

Section S1. COMSOL simulation
Section S2. Spectroscopic measurement and analysis
Section S3. Characterization of morphology
Section S4. Concentration, substrate surface, and MW effects
Section S5. Simulation and experimental results of capillary pen writing
Section S6. Characterization of molecular orientation and packing structures
Section S7. Fabrication and measurement of devices
Section S8. Understanding the molecular origin of flow-induced morphological transition by comparing polymer structures
Section S9. Evidence of $N_{TB}$ mesophase in solution and in deposited thin films
Fig. S1. Sensitivity of regimes to geometric parameters in simulation.
Fig. S2. Complete speed series of velocity fields and strain rates for PII-2T/chloroform blade coating simulations.
Fig. S3. Meniscus height, polymer volume fraction, and evaporative flux profile for PII-2T/chloroform simulations.
Fig. S4. Excited-state electronic structure.
Fig. S5. Normalized solution UV-vis absorption spectra of PII-2T prepared in chloroform with various concentrations from 0.002 to 10 g/liter.
Fig. S6. UV-vis absorption spectra of PII-2T solutions using different MWs.
Fig. S7. UV-vis absorption spectra of PII-2T films printed at various printing speeds.
Fig. S8. PII-2T film preparation for SERS.
Fig. S9. Experimental and calculated Raman intensity.
Fig. S10. Illustration of the main bond stretching assignments for Raman-active vibrational modes.
Fig. S11. Polymer fiber alignment analysis with AFM images as a function of printing speed.
Fig. S12. Top and bottom surface morphology comparison of PII-2T films.
Fig. S13. CPOM images of the films as a function of printing speed.

Fig. S14. CPOM images and thickness of the films as a function of printing speed using various concentrations of PII-2T solutions.
Fig. S15. CPOM images and thickness of PII-2T films as a function of printing speed using various substrate surfaces.
Fig. S16. UV-vis absorption spectra of low-MW PII-2T films printed at various printing speeds.
Fig. S17. Polymer fiber and backbone alignment analysis of low-MW PII-2T films printed at various printing speeds.
Fig. S18. Flow-induced morphological transition for pen-written PII-2T films and velocity and strain rate from computational fluid dynamics simulations.
Fig. S19. Complete speed series of velocity fields and strain rates for PII-2T/o-DCB blade coating simulations.
Fig. S20. Maximum strain rate and inverse residence time as a function of printing speed for PII-2T/o-DCB simulations.
Fig. S21. CPOM images of the capillary pen–written films as a function of printing speed.
Fig. S22. Flow-induced morphological transition in PII-2T films printed using o-DCB solvent.
Fig. S23. Polarized UV-vis absorption spectra and dichroic ratio of PII-2T films printed at various printing speeds with different concentration solutions.
Fig. S24. Comparison and analysis of 2D x-ray diffraction patterns.
Fig. S25. GIXD analysis of PII-2T films obtained at multiple in-plane rotation angles.
Fig. S26. GIXD characterization of PII-2T morphology in the bulk and top surfaces of printed films.
Fig. S27. GIXD characterization of PII-2T films printed at various printing speeds with different solution concentrations.
Fig. S28. Electrical characteristics for as-prepared PII-2T devices without post-thermal treatment.
Fig. S29. Gate voltage–dependent mobility as a function of gate bias, extracted from the transfer curves shown in Fig. 4B.
Fig. S30. Thermal annealing effect of printed PII-2T films.
Fig. S31. Calculated torsion potentials of PII-2T and PTII-2T.
Fig. S32. Normalized solution UV-vis absorption spectra of PTII-2T, DPP-BTz, and DPP2T-TT prepared in chloroform with various concentrations from 0.001 to 10 g/liter.
Fig. S33. Solution and film UV-vis absorption spectra of PII-2T, PTII-2T, DPP-BTz, and DPP2T-TT.
Fig. S34. Morphology characterization of PII-2T, PTII-2T, DPP-BTz, and DPP2T-TT polymer films prepared in each regime.
Fig. S35. Characterization of the polymer film alignment.
Fig. S36. Formation of chiral, liquid crystalline mesophase in PII-2T solutions with increasing concentrations.
Fig. S37. GIXD analysis of twinned morphology in PII-2T films.
Fig. S38. CPOM images of PII-2T twinned morphological films.
Fig. S39. CPOM images of DPP-BTz twinned morphological films.
Fig. S40. Multiple CD measurements of PII-2T and DPP-BTz films printed in evaporation regime.
Table S1. Parameters used in the simulations for PII-2T/chloroform blade coating and PII-2T/o-DCB pen writing.
Legends for movies S1 to S4
References (*42–51*)

**Other Supplementary Material for this manuscript includes the following:**

(available at advances.sciencemag.org/cgi/content/full/5/8/eaaw7757/DC1)

Movie S1 (.avi format). Solution- to solid-state phase transition of PII-2T.
Movie S2 (.avi format). Solution- to solid-state phase transition of PTII-2T.
Movie S3 (.avi format). Solution- to solid-state phase transition of DPP-BTz.
Movie S4 (.avi format). Solution- to solid-state phase transition of DPP2T-TT.

**Section S1. COMSOL simulation**

To model the meniscus guided printing process, we consider a 2D multiphysical model that takes into account solvent vapor diffusion in the gas phase, fluid flow in the solvent meniscus, and 1D convection and diffusion of a non-volatile solute in the meniscus. The meniscus is assumed to be wide enough (in the direction perpendicular to the substrate normal and the printing direction) such that the 3rd dimension can be neglected due to uniformity. The meniscus is also assumed to be isothermal for simplicity. In order to couple the different physics, the kinematic boundary condition is applied at the free surface while also accounting for evaporation. It is assumed that there is only diffusion in the gas phase and that the viscosity of the solvent vapor is much less than that of the solvent in the meniscus, resulting in what is known as a 1.5-sided model. The simulation is set up in a similar manner to Doumenc and Guerrier (42), although here we focus on the resulting flow profile in the meniscus. Derivation of the final governing equations is shown below.

To describe the hydrodynamics, we apply lubrication approximation to simplify the governing equations. Lubrication approximation is valid as long as the meniscus height is much less than the length it spans. The governing equations for fluid flow from continuity and Navier-Stokes are then

$$\mu \frac{\partial^2 u}{\partial y^2} = \frac{\partial p}{\partial x} \tag{1}$$

$$\frac{\partial p}{\partial y} = 0 \tag{2}$$

$$\frac{\partial u}{\partial x} + \frac{\partial v}{\partial y} = 0 \tag{3}$$

where x is along the printing direction, y is along the substrate normal, u and v are the x and y-components of the velocity field, respectively, p is the pressure, and μ is the viscosity . For the fluid domain, the following boundary conditions are applied at the bottom and top interfaces

$$y = 0, \quad u = V_{sub} \tag{4}$$

$$y = h(x,t), \quad \frac{\partial u}{\partial y} = \frac{1}{\mu}\frac{\mathrm{d}\gamma}{\mathrm{d}x} = 0 \tag{5}$$

where equation (4) is the no-slip boundary condition with the substrate translating in the x-direction at a prescribed speed $V_{sub}$ and equation (5) imposes no tangential stress at the meniscus free surface h(x,t) assuming surface tension is constant and the marangoni effect is neglected. Integrating equation (1) and applying these two boundary conditions gives u, the velocity component in the x-direction

$$u = \frac{1}{\mu}\frac{\partial p}{\partial x}\left(\frac{y^2}{2} - hy\right) + V_{sub} \tag{6}$$

Assuming surface tension is constant at the free surface and neglecting marangoni flow and disjoining pressure, the driving force for the flow is (43)

$$\frac{\partial p}{\partial x} = -\gamma\frac{\partial^3 h}{\partial x^3} \tag{7}$$

where γ is the surface tension of the solvent. Equation (7) shows that the driving force is due to capillarity arising from the gradient of meniscus curvature. Substituting equation (7) into (6), gives the x-direction velocity as

$$u = -\frac{\gamma}{\mu}\frac{\partial^3 h}{\partial x^3}\left(\frac{y^2}{2} - hy\right) + V_{sub} \tag{8}$$

Integrating continuity and applying the no penetration boundary condition at the substrate, we get the velocity in the y-direction

$$v = \frac{\gamma}{\mu}\left[\frac{\partial^4 h}{\partial x^4}\left(\frac{y^3}{6} - \frac{hy^2}{2}\right) - \frac{\partial^3 h}{\partial x^3}\frac{\partial h}{\partial x}\frac{y^2}{2}\right] \tag{9}$$

For further derivation it is useful to use the height integrated velocity in the x-direction, which can also be described as a 2D volumetric flux in the x-direction

$$Q(x,t) = \int_0^{h(x,t)} u(x,y,t)\,dy = \frac{\gamma}{\mu}\frac{h^3}{3}\frac{\partial^3 h}{\partial x^3} + V_{sub}h \tag{10}$$

At the free surface, we apply the well-known kinematic boundary condition while also considering mass transport across the interface due to evaporation. At the free surface, the normal component of the interfacial and fluid velocity can be related while accounting for an evaporative mass flux across the interface

$$\vec{v_I} \cdot \vec{n} = \left(\vec{v} - \frac{\vec{J}}{\rho}\right) \cdot \vec{n} \tag{11}$$

where $v_I$ is the velocity of the interface, v is the velocity of fluid at the interface, J is the evaporative flux at the interface, and ρ is the solvent density. Note that J/ρ has units of velocity and can be described as the evaporation velocity $v_{evap}$. The kinematic boundary condition for the free surface with evaporation can be shown to be

$$\frac{\partial h}{\partial t} + u\frac{\partial h}{\partial x} = v - v_{evap} \tag{12}$$

Integrating the continuity equation (3) over height and substituting the 2D volumetric flux (10) and the kinematic boundary condition (12) gives a mass balance for the meniscus in terms of its height, h(x,t)

$$\frac{\partial Q(x,t)}{\partial x} + \frac{\partial h}{\partial t} = -v_{evap} \tag{13}$$

The evaporation velocity is determined by the diffusive flux at the free surface, which is the evaporative flux. Diffusion in the gas phase is simply governed by Fick's Law

$$\frac{\partial c}{\partial t} = D_g\left(\frac{\partial^2 c}{\partial x^2} + \frac{\partial^2 c}{\partial y^2}\right) \tag{14}$$

where c(x,y,t) is the concentration of solvent vapor in the gas domain and $D_g$ is the diffusion coefficient for the solvent vapor in air. The gas domain is a rectangular domain above the meniscus, which is considered to be flat for the purposes of evaporation and vapor diffusion. This is valid as long as lubrication approximation is used to describe the hydrodynamics of the meniscus. At the bottom boundary which represents the meniscus free surface the solvent

vapor is saturated and at the top boundary the concentration is set to 0. At the vertical boundaries perpendicular to the substrate there is no flux. In order to model the spatial dependence of the evaporative flux at the meniscus, the saturation concentration can be modified by an activity coefficient which depends on the volume fraction of non-volatile solute in the meniscus (42), φ(x,t). The boundary conditions in the gas domain are therefore

$$x = 0 \text{ and } L, \quad \frac{\partial c}{\partial x} = 0 \tag{15}$$

$$y = H, \quad c = 0 \tag{16}$$

$$y = 0, \quad c = a(\phi)\frac{p_{sat}(T)M}{RT} \tag{17}$$

where M is the molar mass of the solvent. The solute concentration dependence of the activity coefficient can be described by the Flory-Huggins Law (42), which is

$$a(\phi) = (1 - \phi)\exp\left(\phi + \chi\phi^2\right) \tag{18}$$

where χ is the Flory-Huggins interaction parameter and can be roughly estimated from solubility parameters of the polymer and solvent using (44)

$$\chi = \frac{V_m}{RT}\left(\delta_{polymer} - \delta_{solvent}\right)^2 + 0.34 \tag{19}$$

where $V_m$ is the molar volume of the solvent and δ is the solubility parameter for either the polymer or solvent. Solving for the concentration profile in the gas domain gives the evaporation velocity at the free surface which can then be used for the mass balance in the meniscus (13)

$$v_{evap}(x,t) = -\frac{D_g}{\rho}\frac{\partial c}{\partial y}\Big|_{y=0} \tag{20}$$

Finally, a non-volatile solute is modeled within the meniscus that can be transported by both convection and diffusion. By carrying out a mass balance across the meniscus it can be shown that the solute mass balance is described by the following equation

$$\frac{\partial(\phi h)}{\partial t} + \frac{\partial(\phi Q)}{\partial x} = \frac{\partial}{\partial x}\left(hD\frac{\partial \phi}{\partial x}\right) \tag{21}$$

where D is the diffusion coefficient of the polymer in the solvent. Considering the rigidity of conjugated polymers, the diffusion coefficient can be roughly estimated by formulas developed for rigid rods (45). Equations (13), (14), and (21) form a system of PDE's that govern the multiphysical processes occurring in meniscus guided printing. The boundary conditions for the meniscus domain at the left and right boundaries are (42)

$$x = 0, \quad h = h_0, \ \frac{\partial^2 h}{\partial x^2} = C_0, \ \phi = \phi_0 \tag{22}$$

$$x = L, \quad \frac{\partial h}{\partial x} = 0, \ \frac{\partial^2 h}{\partial x^2} = 0, \ \frac{\partial \phi}{\partial x} = 0 \tag{23}$$

Solving the system of equations gives three dependent variables: the meniscus height profile, h(x,t), the solute volume fraction profile, φ(x,t), and the solvent vapor concentration profile in the gas domain, c(x,y,t). The final system of governing equations are solved by FEM using the user-defined PDE interface in COMSOL Multiphysics (versions 5.2a and 5.3a). The time-dependent simulation is carried out until the meniscus reaches a steady state and no longer changes considerably with time. From the meniscus height profile, h(x,t), and its higher order spatial derivatives, the velocity field and strain rates within the meniscus can be calculated. A table of values for the parameters used in the simulations is shown below. A concentration-dependent viscosity model up to near solid conditions ($\varphi = 0.9$) is required. Considering the small amounts of conjugated polymer available and the high volatility of chloroform, viscosity measurements up to extremely concentrated conditions are difficult to perform. Instead we use the viscosity model for poly(isobutylene)/toluene used by Doumenc and Guerrier (42). Usage of different viscosity models only has a significant effect on shifting the LL regime while having a minimal effect on the evaporation regime. Nonetheless, we find that the substitution is sufficient as film thicknesses and regimes predicted from simulation match well with those measured experimentally.

**Table S1. Parameters used in the simulations for PII-2T/chloroform blade coating and PII-2T/o-DCB pen writing.**

| Parameter | Polymer/Chloroform | Polymer/o-DCB |
|---|---|---|
| Surface tension, $\gamma$ (mN/m) | 26.67 | 36.61 |
| Molar mass, $M$ (g/mol) | 119.38 | 146.998 |
| Density, $\rho$ (kg/m$^3$) | 1,490 | 1,300 |
| Solvent-air diffusivity, $D_g$ (m$^2$/s) | $1 \times 10^{-5}$ | $7 \times 10^{-6}$ |
| Vapor pressure, $p_{sat}$ (Pa) | 26,000 | 1,400 |
| Polymer-solvent diffusivity, $D$ (m$^2$/s) | $1 \times 10^{-11}$ | $1 \times 10^{-11}$ |
| Flory interaction parameter, $\chi$ | 0.35 | 0.38 |
| Initial meniscus height, $h_0$ (µm) | 100 | 100 |
| Initial meniscus curvature, $C_0$ (1/mm) | 2 | 2 |
| Initial polymer volume fraction, $\phi_0$ | 0.01 | 0.03 |
| Gas domain height, $H$ (mm) | 2 | 1 |
| Gas domain length, $L$ (mm) | 1 | 1 |
| Temperature, $T$ (K) | 298 | 333 |

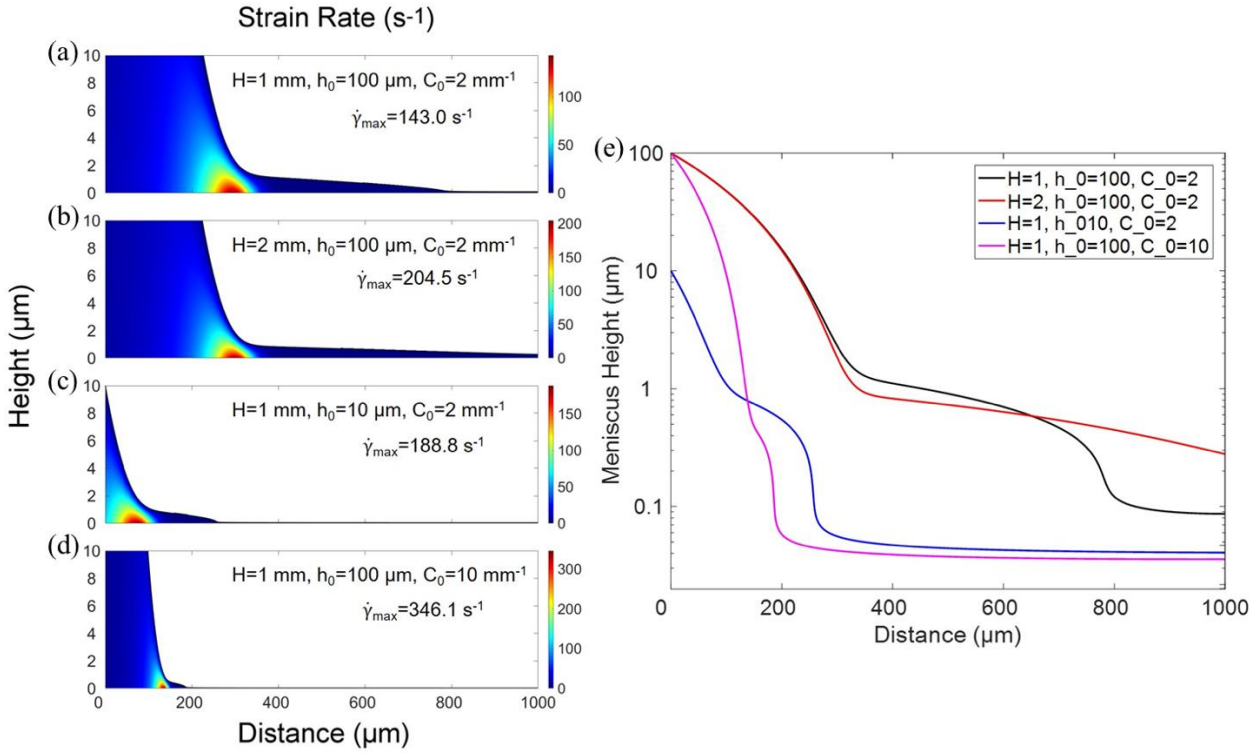


**Fig. S1. Sensitivity of regimes to geometric parameters in simulation.** (a) Main conditions ($H$ = 1 mm, $h_0$ = 100 μm, $C_0$ = 2 mm$^{-1}$, $\gamma_{max}$ = 143 s$^{-1}$) used in PII-2T/o-DCB simulation at 250 μm/s. This speed was chosen because it occurs in the middle of the transition regime, where the length of the dragged out meniscus is especially sensitive to changes in conditions. The transition regime itself is a narrow range of speeds due to the fact that the drag out length increases superlinearly with printing speed until it reaches the end of the simulation box. (b) Increasing the height of the gas domain, $H$, from 1 mm to 2 mm shifts the speed from the transition regime to the Landau-Levich regime. This is expected as increasing the height of the gas domain reduces the concentration gradient and subsequently reduces the evaporative flux. Therefore, the viscous forces present become stronger relative to the reduced evaporation and the regimes transitions shift down to lower speeds. Considering the speed is now further into the Landau-Levich regime, the strain rate within the meniscus is higher. (c) The initial height, $h_0$, is reduced from 100 μm to 10 μm. Here, there is minimal difference between the base conditions in (a). We see that the meniscus still exhibits partial drag out indicating it is still within the transition regime. The maximum strain rate is slightly higher as well. Considering the results are still quite similar, this suggests that properties in the bulk of the meniscus remains nearly constant until reaching close to the contact line. In other words, for the base case where $h_0$ = 100 μm, the conditions at x = 226 μm (where h = 10 μm) are still very similar to the boundary conditions imposed at x=0. As a result, starting the meniscus at $h_0$ = 10 μm and imposing the same boundary condition leads to very similar results. (d) The initial curvature, $C_0$, is increased from 2 mm$^{-1}$ to 10 mm$^{-1}$. As expected, the overall meniscus length is shortened due to the increased curvature imposed at x=0, causing the bulk curvature to intercept the substrate earlier. The maximum strain rate has increased significantly by about 2.4x. This is likely due to the fact that the meniscus height profile, h(x,t), and its higher order derivatives are used to determine the velocity field and strain rate. The increased curvature increases the value of the second spatial derivative of h(x,t). The dominant term in

the strain rate tensor is du/dy which depends on the third derivative of h(x,t). The larger change in curvature from the bulk of the meniscus to the dragged out length where the curvature is nearly zero results in a larger strain rate. Despite this, the presence of the partially dragged out meniscus indicates that this condition is still within the transition regime and may only be slightly shifted. (e) Meniscus height profiles for base condition (black) and three variations described here (red, blue and magenta). The presence of a second inflection point in the height profile is indicative of a partially dragged out liquid film from the meniscus. This is seen in all cases except when increasing the height of the gas domain, suggesting that changes to initial height and curvature only shift the regimes slightly and overall trends remain the same.

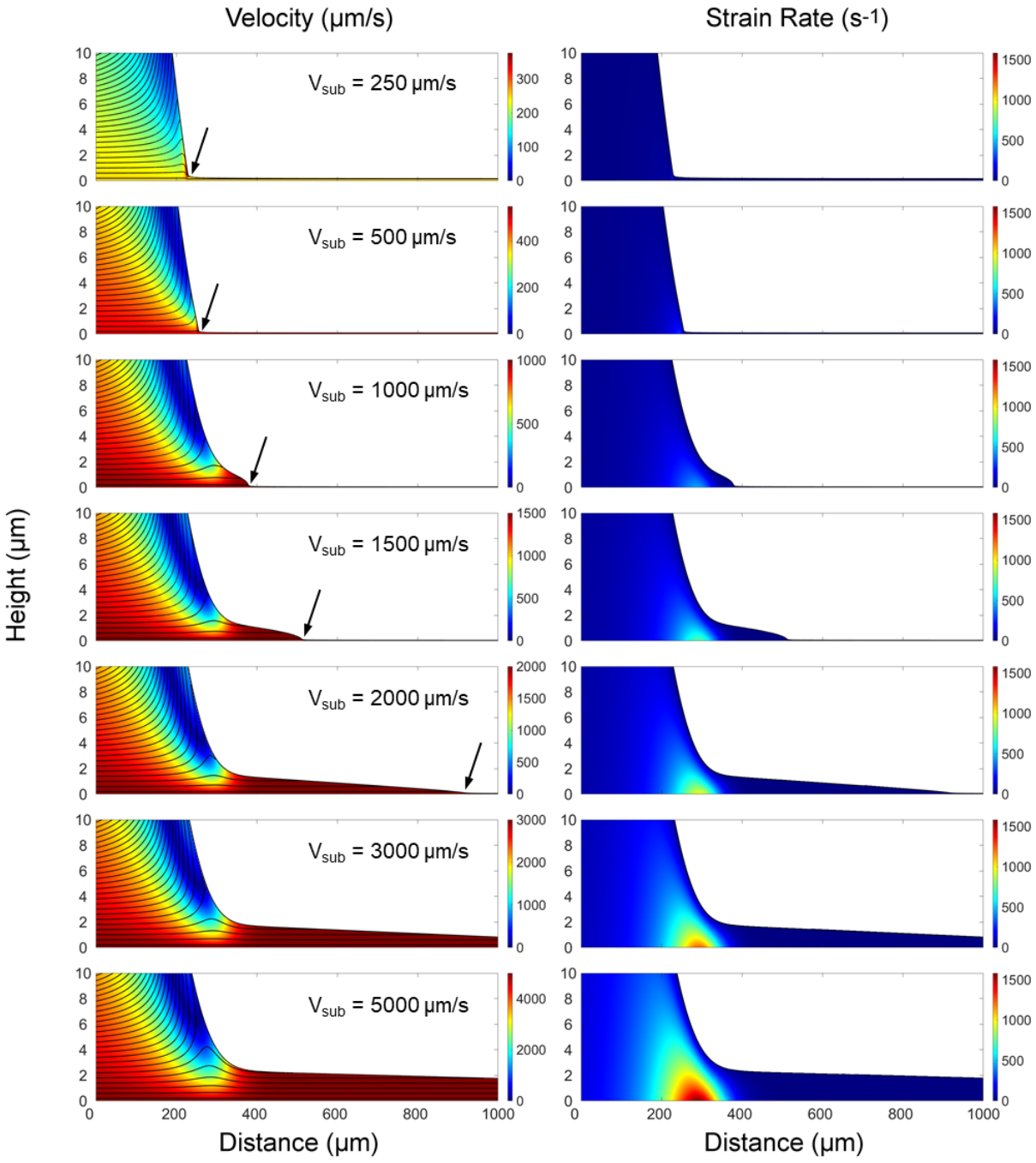


**Fig. S2. Complete speed series of velocity fields and strain rates for PII-2T/chloroform blade coating simulations.** (left) Velocity magnitude and streamlines for all printing speeds. The meniscus contact line is noted by black arrows. Evaporation dominates at low speeds resulting in a short meniscus of constant curvature. The transition regimes starts after 500 μm/s where the meniscus begins to be dragged out. After 2000 μm/s the dragged out liquid film reaches the end of the simulation box suggesting that the meniscus is very near or in the LL regime. (right) Strain rate for all printing speeds. Shear rates are low at low speed but begin to rise rapidly in the transition regime at 1000 μm/s. The shear rate continues to increase into the LL regime, although the residence time is exceptionally long due to the dragged out liquid film which dries quiescently at high speeds. Color bar for all speeds ranges from 0 $s^{-1}$ to 1583 $s^{-1}$, the maximum strain rate for 5000 μm/s.

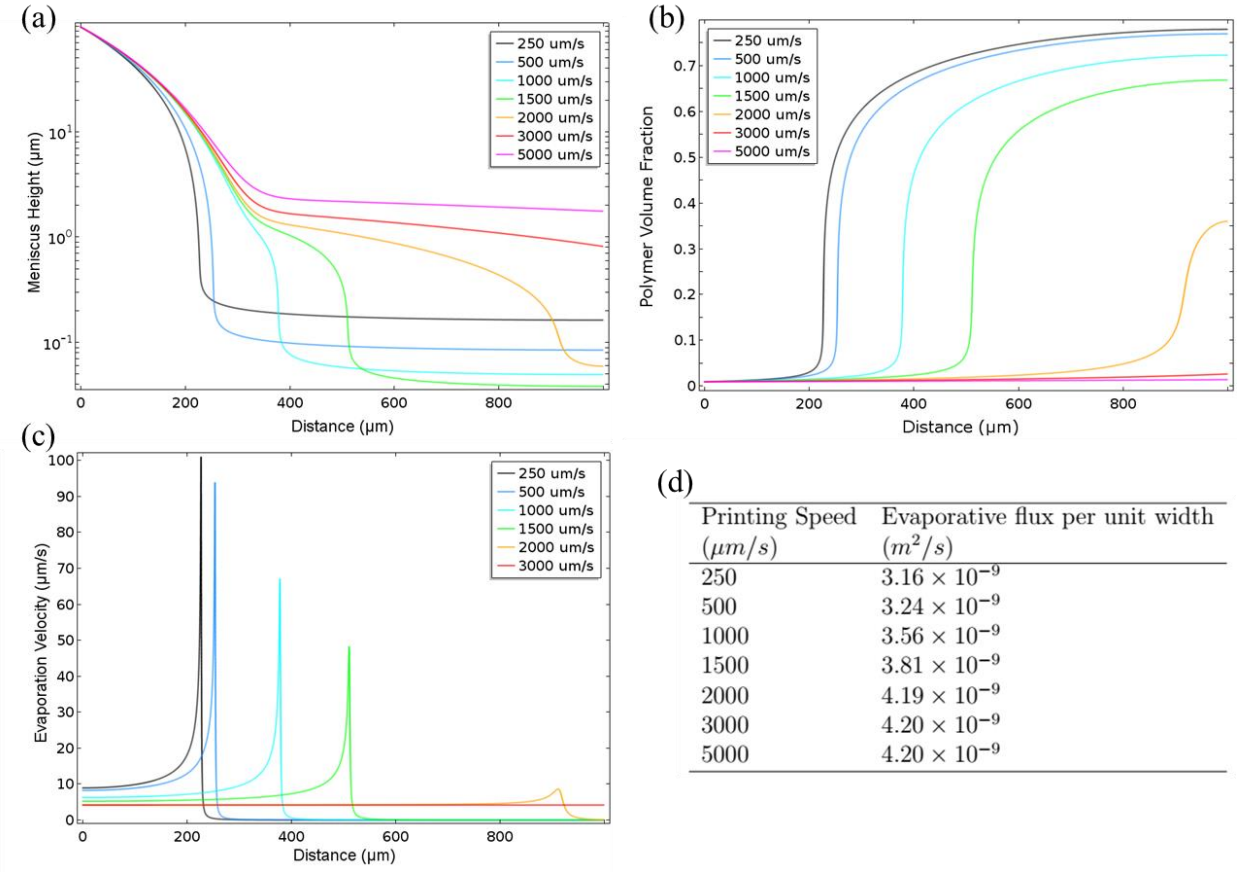


| Printing Speed $(\mu m/s)$ | Evaporative flux per unit width $(m^2/s)$ |
|---|---|
| 250 | $3.16 \times 10^{-9}$ |
| 500 | $3.24 \times 10^{-9}$ |
| 1000 | $3.56 \times 10^{-9}$ |
| 1500 | $3.81 \times 10^{-9}$ |
| 2000 | $4.19 \times 10^{-9}$ |
| 3000 | $4.20 \times 10^{-9}$ |
| 5000 | $4.20 \times 10^{-9}$ |

**Fig. S3. Meniscus height, polymer volume fraction, and evaporative flux profile for PII-2T/chloroform simulations.** (a) log-linear plot of the meniscus height profile h(x,t) for all speeds. In the evaporation regime, the height profile has an inflection point that occurs at the contact line. In the transition regime, two inflections points are seen in the height profile with the first corresponding to the start of the partially dragged out liquid film and the second corresponding to the contact line. In the LL regime, there is only one inflection point in the height profile that corresponds to the start of the dragged out liquid film. There is no contact line in the LL regime as the meniscus reaches the end of the simulation box. (b) The polymer (solute) volume fraction profile φ(x,t) for all speeds. The inflection point that occurs at the sudden rise in polymer concentration corresponds to the contact line where the meniscus transitions into a deposited film. In the LL regime, there is no rise in polymer concentration since a bulk liquid film is dragged out of the meniscus. (c) The evaporation velocity profile $v_{evap}(x,t)$ for all speeds. The peak evaporation occurs at the contact line. In the LL regime, the evaporation profile is a constant low value since there is no contact line and only a bulk liquid film. The evaporation profile for 5000 μm/s (not pictured) is practically the same as that of 3000 μm/s. The peak evaporation and inflection points in the height and polymer concentration profile occur at the same position indicating the contact line. (d) The integrated evaporation velocity over the length of the simulation box shows that while printing speed increases by over a magnitude, the evaporation rate remains similar.

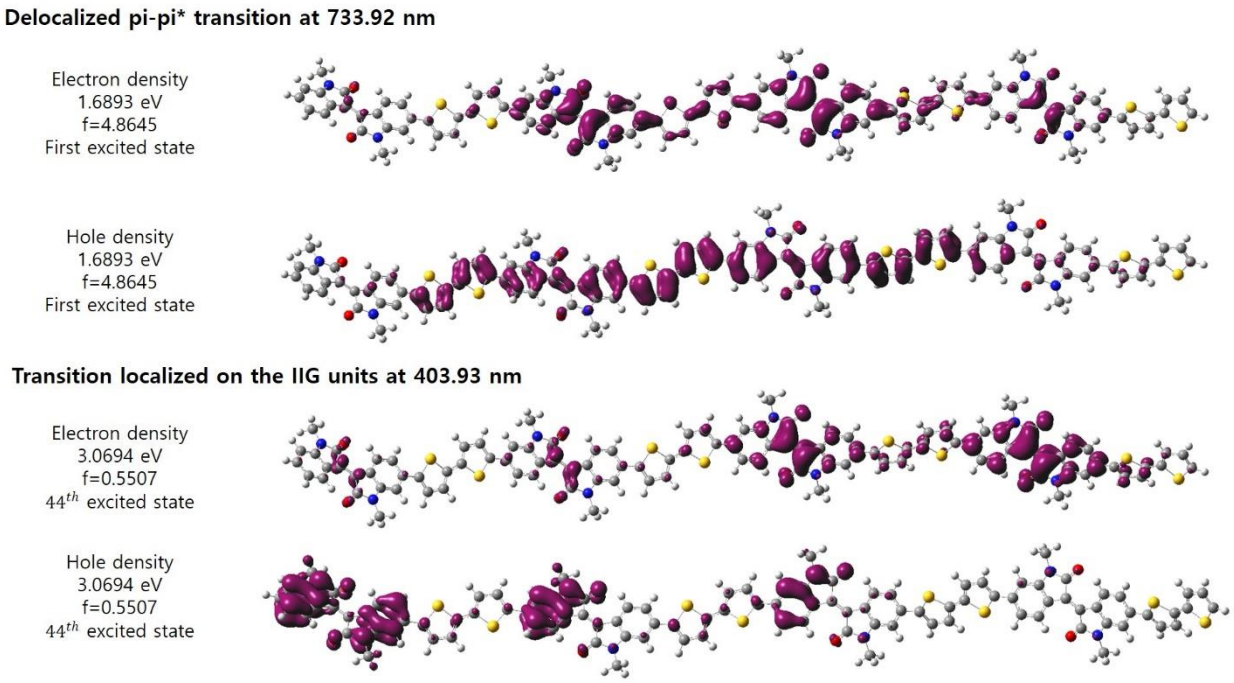


**Fig. S4. Excited-state electronic structure.** The absorption spectra in the main text (Fig. 2C) for SYN and ANTI configurations were obtained at the time dependent density functional theory (TD-DFT) level with global hybrid function B3LYP in conjunction with a 6-31G(d,p) basis set. The species were fully relaxed at the density functional theory (DFT) level with the same hybrid functional and basis set before running TD-DFT. Long alkyl side chains have been replaced by $CH_3$ to save computational cost. This should not significantly affect the results considering charge transport primarily occurs along the backbone.

The optical absorption spectrum adopts a 'camel back' shape with two main bands. We show above the molecular orbitals involved in the two transitions in the case of a tetramer (in an ANTI configuration). The low-energy $S_0 \rightarrow S_1$ excitation entails molecular orbitals that are delocalized through the entire π-system, hence prompting a large oscillator strength *f*, but with higher (lower) electron density on the IIG acceptor (2T donor) units, conveying an intramolecular charge-transfer character and a low excitation energy. The second main absorption band instead consists of an electronic transition between molecular orbitals that are very much confined on the IIG units, thus characterized by a higher excitation energy and a lower oscillator strength. Because of their different nature, the relative energy separation and intensity ratio between the two main optical absorption bands are both highly sensitive to the amount of π -delocalization, which is primarily controlled by the conformation of the conjugated polymer backbones.

**Section S2. Spectroscopic measurement and analysis**

In order to verify whether the measured film absorption coefficients result from intrinsic molecular properties or aggregation UV-Vis absorption spectroscopy measurements were performed over a range of PII-2T concentrations (0.002 to 10 g/L) prepared with chloroform. The spectral shape was insensitive to solution concentration as shown in fig. S5. Also, we compared the UV-Vis absorption spectra of different molecular weight (MW) PII-2T for both solutions and films. The comparison of normalized high and low MW PII-2T solution UV-Vis absorption spectra shows a slightly red-shifted 0-0 peak and an increased ratio of $A_{0\text{-}0}/A_{0\text{-}1}$ for high MW PII-2T (fig. S6). This change can be attributed to either more J-aggregation or more planarized conformation present for the HMW than LMW PII-2T. Because no significant aggregation arose in solution as shown in fig. S5, this result would more likely be caused by a conformational difference. Moreover, the molar absorption coefficient of HMW PII-2T is about three times higher than that of LMW PII-2T (fig. S6), which indicates that HMW PII-2T likely forms a more favorable conformation for optical transitions as described previously (*26*). These observations suggest that the absorption phenomena of the printed films are not the result of chain aggregation but molecular conformation instead.

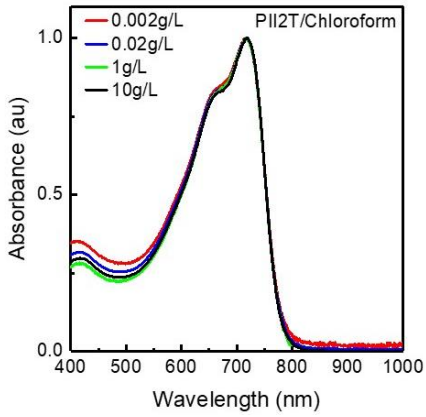


**Fig. S5. Normalized solution UV-vis absorption spectra of PII-2T prepared in chloroform with various concentrations from 0.002 to 10 g/liter.** The diluted solutions (0.002 and 0.02 g/L) were measured with a 1-cm-path-length cuvette, and the concentrated solutions (1 and 10 g/L) were measured with a 10-μm-path-length cuvette.

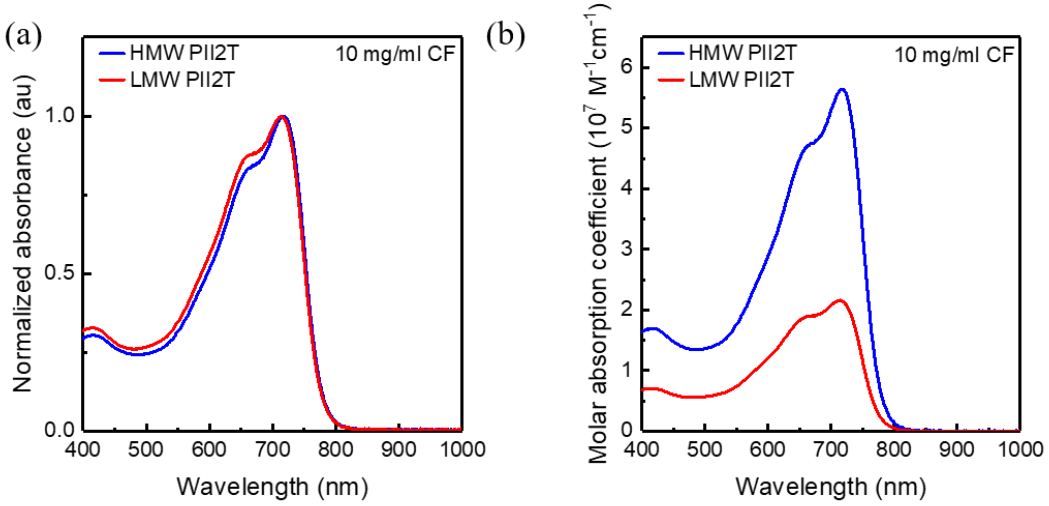


**Fig. S6. UV-vis absorption spectra of PII-2T solutions using different MWs.** (a) Normalized solution UV-Vis absorption spectra of PII-2T prepared in chloroform with different MW. The 0-0 peak is slightly red-shifted from 713 to 717 nm and the peak intensity ratio of $A_{0\text{-}0}/A_{0\text{-}1}$ is also slightly increased from 1.14 to 1.19 for high MW PII-2T. (b) Molar absorption coefficient of high MW and low MW PII-2T. The coefficient was calculated per molar concentration using $M_W$ (HMW) = 715,643 Da and $M_W$ (LMW) = 291,735 Da, respectively.

Because the absorption coefficient of a donor-acceptor conjugated polymer is dependent on the orbital overlaps between hole and electron wave functions (*26*), the trend in absorption coefficient as a function of printing speed implies that fluid flow is able to influence the geometric and electronic structures of these films. The higher absorption coefficient was observed for the PII-2T films printed in the transition regime (~1 mm/s) where there is high strain rate and relatively low residence time. In addition to the absolute magnitude of absorption coefficient, the absorption spectra shape, determined by the transition energy distribution, was used as an indication of flow-induced molecular conformation modulation. Figure S7 shows the normalized UV-Vis spectra of PII-2T films along with absorption intensity ratios of the 0-0 to 0-1 transition and the spectral positions of the 0-0 transition as a function of printing speed. We found the intensity ratio of $A_{0\text{–}0}/A_{0\text{–}1}$ rapidly increased and the

peak broadening substantially decreased as the films were printed from the evaporation to the transition regime. The peak position of 0–0 (717–719 nm) is only slightly changed across the printing speeds when compared to solution (719 nm) except for the red shift for 0.1 mm/s (~724 nm). Previous studies have demonstrated that the absorption cross-section is redistributed from lower to higher vibronic transitions as the effective conjugation length is reduced through increasing torsional disorder (*28*). This is also accompanied with an increased spectral broadening of the peaks. Thus, the concurrent observation of peak broadening together with reduced $A_{0-0}/A_{0-1}$ intensity ratio clearly points to reduced conjugation length likely driven by increased conformation freedom in films formed in evaporation regime. In contrast, the polymer backbones are expected to adopt a more planar conformation when strong strain is applied in the transition regime.

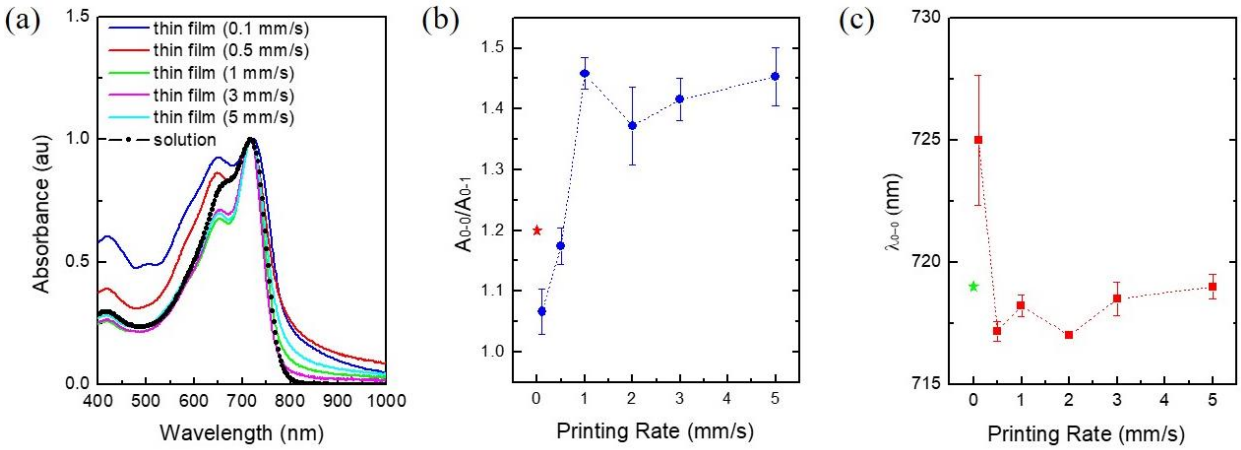


**Fig. S7. UV-vis absorption spectra of PII-2T films printed at various printing speeds.** (a) Normalized solution (black line), and film UV-Vis absorption spectra of PII-2T. The solutions are prepared in chloroform at 10 mg/ml. The films were prepared on an OTS-functionalized glass substrate by blade coating at various printing speeds. The solution measurement was carried out with a short-path-length cuvette of 10 μm. The peak broadening decreases with increasing printing speed. (b) The 0-0/0-1 transition intensity ratio with the peak absorbance obtained at ~719 nm (0–0) and ~650 nm (0–1), respectively as a function of printing speed. (c) The peak position of the 0-0 transition as a function of printing speed. The star mark indicates the peak ratio and position obtained from the solution spectrum. The dashed lines serve as a guide for the trend.

The semiconducting properties of conjugated polymers are derived from their delocalized π-electronic structure, which can be probed very effectively using Raman spectroscopy (*29*). We can therefore use this technique to elucidate how flow causes redistribution of the π-electron density on the polymer molecule. First we prepared PII-2T films printed on an ultra-thin (~9 nm) gold layer as illustrated in fig. S8 (a) to take advantage of surface-enhanced Raman scattering (SERS) (46). The gold layer was deposited on the $SiO_2$ substrate by thermal evaporation at a rate of 0.5 Å $s^{-1}$. The PII-2T films were then printed using blade coating at printing speeds of 0.1, 1 and 10 mm/s, corresponding to the evaporation, transition, and LL regimes. The morphology of the films printed on gold (fig. S8 (b)) are similar to those prepared on an OTS-functionalized surface.

The Raman spectra were measured using 532 nm excitation to achieve a strong Raman signal with low background photoluminescence. The measured Raman spectra and DFT frequency analysis are shown in fig. S9 for the films printed in the three regimes. We consider vibrational modes in the range 1300–1700 $cm^{-1}$, which correspond to carbon bond stretching. For comparing Raman shifts and relative peak intensity we normalized the spectra by the strongest peak around 1435 $cm^{-1}$. The most interesting modes are the delocalized C=C stretching over thiophene and phenyl rings (1435 $cm^{-1}$), strong localized central C=C stretching between the two indolinones of isoindigo (1531 $cm^{-1}$), and strong C=C stretching on localized phenyl rings (1610 $cm^{-1}$) (see fig. S10 for a detailed illustration). The notable difference between spectra is the enhanced relative intensity of the modes at 1531 and 1610 $cm^{-1}$ (IIG acceptor) and the slight up shift of the 1531 $cm^{-1}$ peak for the 1 mm/s printed film. Since the Raman scattering intensities in conjugated polymers arise from the polarizability of the π-electrons, they provide evidence that the planarized isoindigo ring unit has an increased π-electron density relative to the donor unit. Moreover, the shift to higher frequency indicates an increased effective force constant for vibration of this bond. This can be understood as an

increase in the π-bonding strength in the benzene ring, which suggests an increased π-electron density.

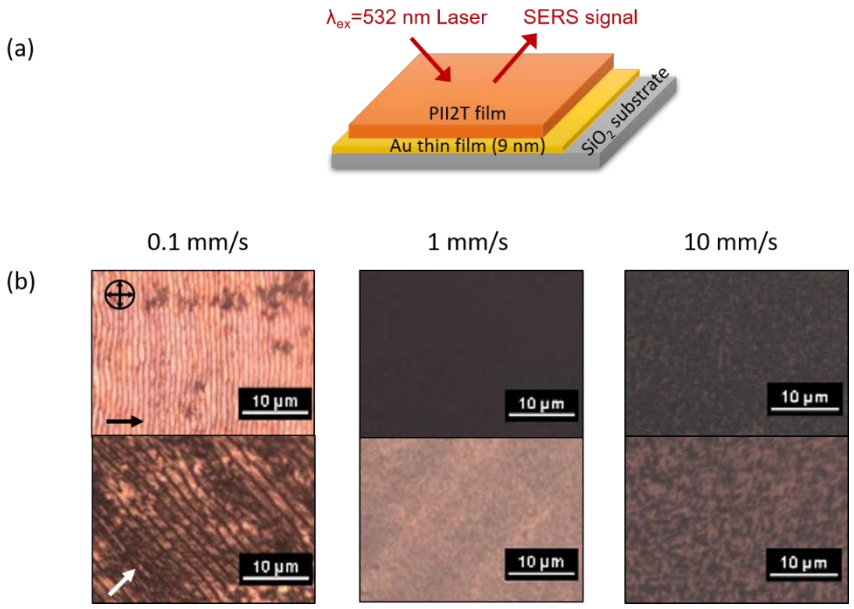


**Fig. S8. PII-2T film preparation for SERS.** (a) Schematic illustration of printed PII-2T films for SERS measurement. (b) CPOM images of PII-2T films printed on gold. The arrows indicate the printing direction. The 0.1 mm/s-printed film shows clear twinned morpology with strong birefringence, exhibiting higher intensity when the printing direction is oriented parallel to one of the crossed polarizers. The 1 mm/s-printed film shows a relatively smooth morphology with birefringence but exhibits higher intensity when the printing direction is oriented 45° between the crossed polarizers, indicating high alignment parallel to the printing direction. At 10 mm/s we see that the film still exhibits higher intensity at 45°, however the birefringence is considerably weaker indicating a broader distribution of orientation. These observations are consistent with those formed on OTS-functionalized substrates.

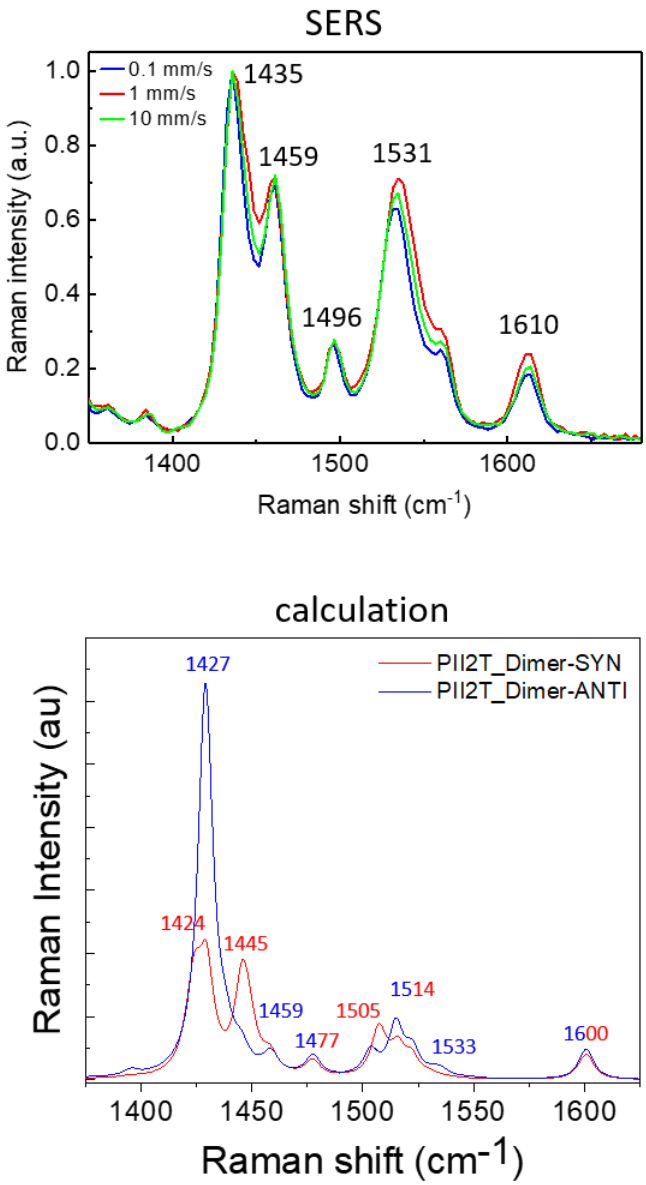


**Fig. S9. Experimental and calculated Raman intensity.** (Top) SERS measurement and (Bottom) calculated Raman intensity of PII-2T films. The measured spectra are normalized to strongest peak (1435 $cm^{-1}$). Note that the trends of the calculated results are in accordance with the experimental results, even though their values are not exactly identical due to the limitations of the DFT models with trimmed alkyl side chains and a limited backbone length.

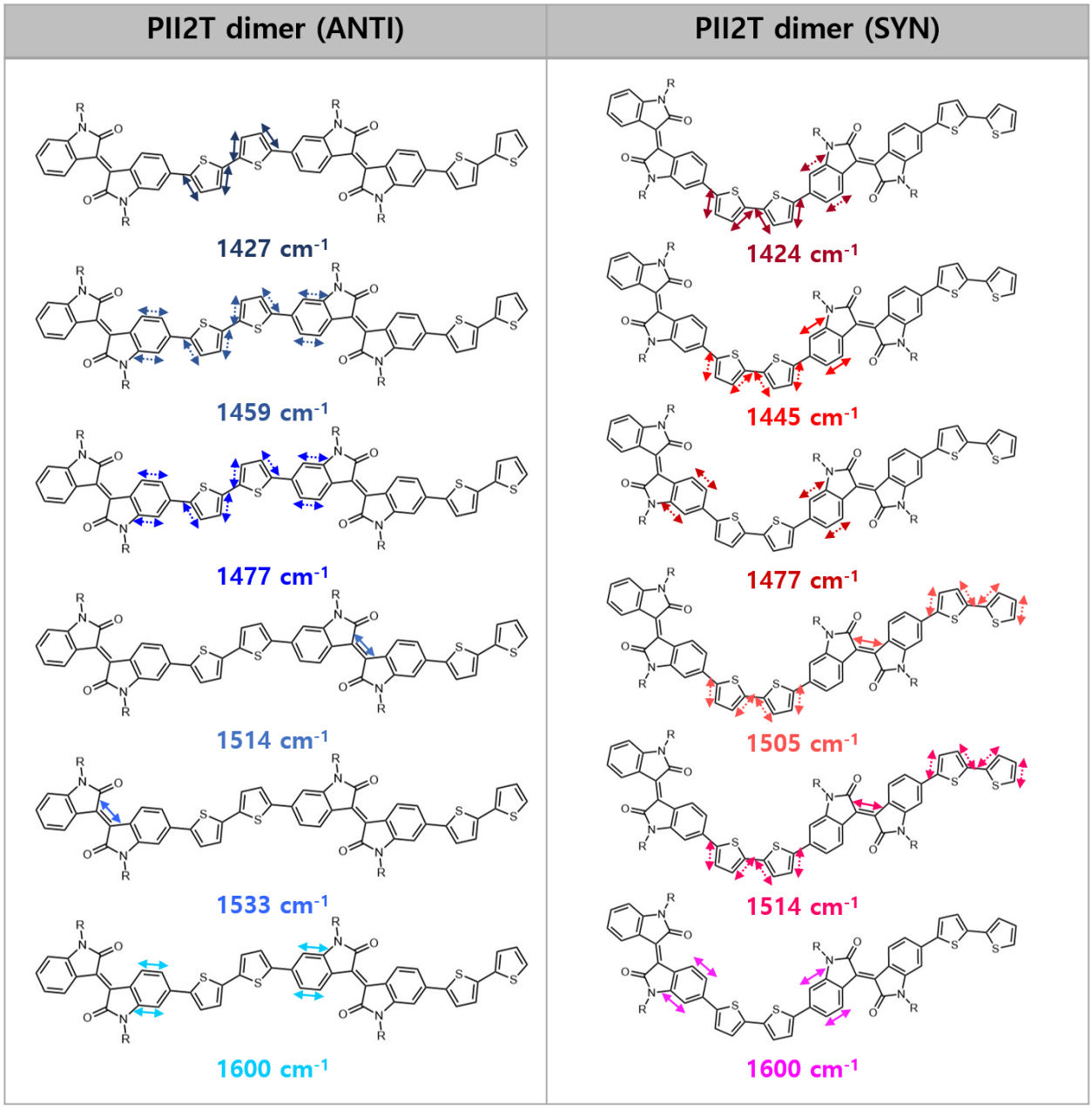


**Fig. S10. Illustration of the main bond stretching assignments for Raman-active vibrational modes.** The peak position values are obtained from SYN and ANTI conformations. Solid and dotted arrows indicate the relatively stronger and weaker stretching modes, respectively.

## Section S3. Characterization of morphology

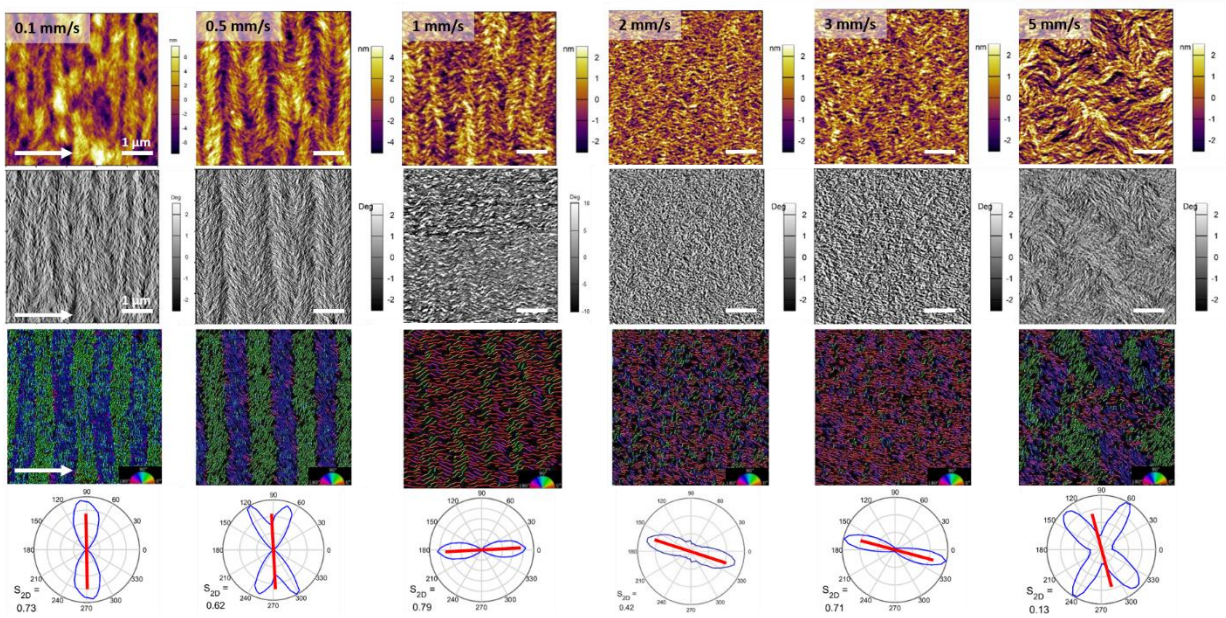


**Fig. S11. Polymer fiber alignment analysis with AFM images as a function of printing speed.** The first two rows show the AFM height and phase images of PII-2T films printed at 0.1−5 mm/s. All scale bars are 1 μm. The arrows indicate the printing direction. The third row represents false color orientation maps extracted from the respective phase images using the GT Fiber software as demonstrated previously (31). The color wheel at the bottom right corner indicates the orientation range from 0 to 180°. In the evaporation regime, the polymer fibers are oriented nearly perpendicular (60 and 120 degrees) to the printing direction with their orientation gradually becoming more parallel to printing direction with increasing speed. In the transition regime, the fibers are mostly oriented parallel to the printing direction due to the strong strain rate. In Landau-Levich regime, the fibers are less oriented because long residence times in solution allow molecular re-orientation prior to deposition. The fourth row shows the orientation distribution with the orientation order parameter of $S_{2D}$ extracted from each orientation map. The $S_{2D}$ is defined as $S_{2D} = 2\langle\cos^2\theta_n\rangle - 1$ where $\theta_n$ is the angle between an individual fiber pixel and the overall director ($n$) of image, i.e. the average orientation (red line in the plots). Thus, $S_{2D}$ varies between 0 and 1 depending on how much average orientation deviates from the director, with 0 denoting completely random and 1 indicating perfectly oriented to the director. The relatively high $S_{2D}$ of 0.73 for the 0.1 mm/s image indicates the fiber orientation is narrowly distributed perpendicular to the printing direction. Similarly, the high $S_{2D}$ of 0.79 for the 1 mm/s means the fibers are mostly oriented parallel to the printing direction. However, a less ordered orientation is shown for the 5 mm/s with a low $S_{2D}$ of 0.13.

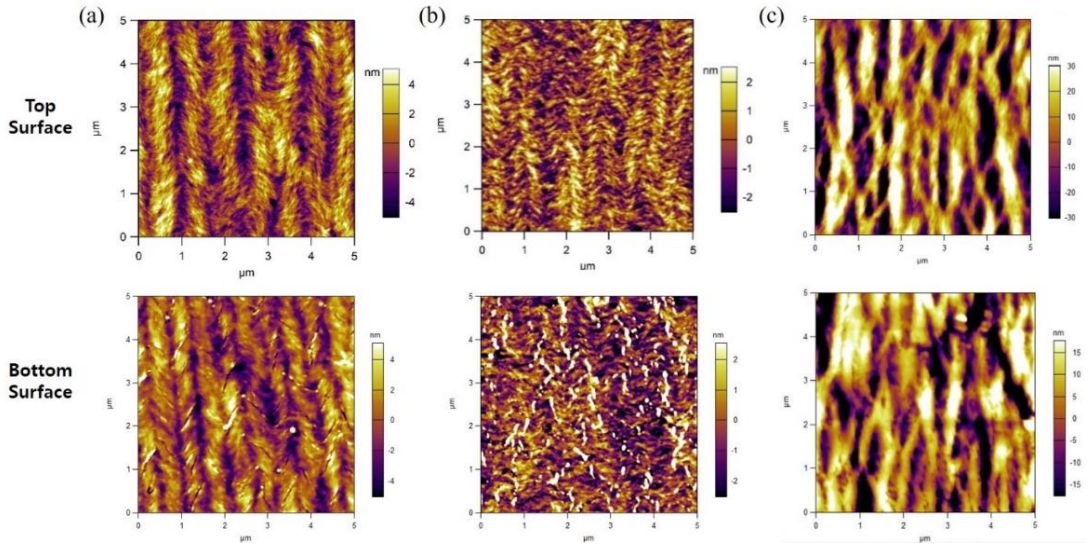


**Fig. S12. Top and bottom surface morphology comparison of PII-2T films.** AFM topographic images of PII-2T films blade coated at (a) 0.5 mm/s and (b) 1 mm/s using 10 mg/ml chloroform solution and the film pen written at (c) 0.1 mm/s using 30 mg/ml o-DCB solution. The first row shows the top interface (film–air interface) morphology, and the second row shows the bottom interface (film–substrate interface) morphology. The samples for bottom interface were prepared by laminating the polymer films using PDMS stamps. The AFM shows the similar interfacial morphology at the top and the bottom surfaces.

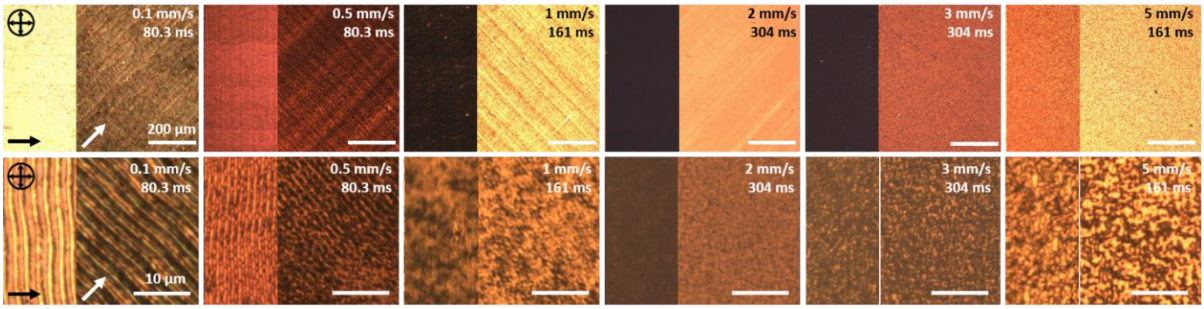


**Fig. S13. CPOM images of the films as a function of printing speed.** 10x (top row) and 200x (bottom row) magnified CPOM images correspond to films with the printing direction oriented 0° and 45° with respect to the polarizer axis. The arrows indicate the printing direction and the crossed arrows indicate the orientation of the crossed polarizers. The printing speed and exposure time of each image are denoted in the upper right corner. Birefringence in the films is clearer at 10x magnification while morphology is more easily seen at 200x magnification. Quantitative birefringence characterization is shown in the main text (Fig. 2G), which was obtained by extracting the average intensity from multiple data points of 10x images captured with a consistent exposure time of 147 ms.

## Section S4. Concentration, substrate surface, and MW effects

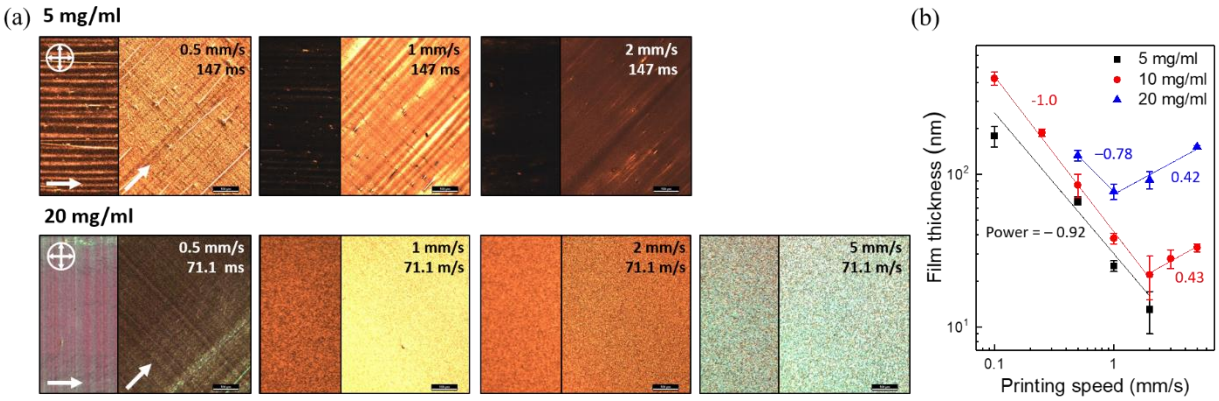


**Fig. S14. CPOM images and thickness of the films as a function of printing speed using various concentrations of PII-2T solutions.** (a) The CPOM images correspond to films with the printing direction oriented 0° and 45° with respect to the polarizer axis. The PII-2T films were printed with 5 or 20 mg/ml chloroform solutions. The arrows indicate the printing direction, and the crossed arrows indicate the orientation of the crossed polarizers. The printing speed and exposure time for the images are denoted in the upper right corner. All scale bars are 100 μm. Note that the light exposure time for capturing images is consistent for direct comparison over the films. The optical birefringence between the images captured at 0º and 45º provides a qualitative measure of overall chain alignment. Notably, the images of printed films at 1 mm/s show a dramatic birefringence for both 5 and 20 mg/ml PII-2T solutions, similar to the results (fig. S13) for 10 mg/ml. The transition regime (~1 mm/s), in which polymer is aligned by strong strain rate is also observed for the various concentrations. It is noted that the regimes are shifted due to changes in the viscosity which depend on concentration. (b) Double logarithmic plots of PII-2T film thickness as a function of printing speed for various concentrations of PII-2T solution. Two regimes, evaporation and Landau-Levich, are clearly identified based on the film thickness. Particularly, the evaporation regime is well defined by the relationship between film thickness ($h$) and printing speed ($v$) demonstrated by equation $h = (CQ_{evap}/\rho L)\, v^{-1}$, where $C$, $Q_{evap}$, $\rho$ and $L$ are the mass concentration, evaporation rate, density and the width of film, respectively (*25*). The exponent for each power law fit is indicated in the plot. The values of -0.92 and -1.0 from the 5 and 10 mg/ml solutions are in good agreement with the mass balance equation (slope = -1) in evaporation regime. The value of -0.78 is slightly deviated for 20 mg/ml probably because of recirculation in the meniscus and the lack of enough data points. A different dependency (slope = 0.43 and 0.42 for the 10 and 20 mg/ml solution, respectively) is shown in Landau-Levich regime, where a thick liquid film is dragged out and the film thickness increases with the printing speed(*25*). It is noted that only a few measurements could be taken for a small range of printing speeds the 5 mg/ml solution because the low viscosity solution dewets on the lyophobic OTS surface forming an unstable meniscus. The concentration-dependent film thickness as a function of printing speed shows two distinct regimes based on the relative dominance of evaporation and viscous forces with the transition regime in between being defined by the meniscus shape and flow profile which affects the polymer conformation and film morphology.

Substrate wettability can affect the morphology of printed films. For an evaporating meniscus the wettability of the liquid and the subsequent contact angle can change the evaporation rate for various reasons. Generally, the evaporative flux increases with decreasing contact angle. This is due to increased meniscus free surface area, faster heat transfer from the substrate due to thinner meniscus height, and enhanced diffusion of solvent vapor near the contact line. What is also typically seen in these cases is a large increase in evaporative flux near the contact line but only a slight increase in the integrated evaporative flux over the free surface. As a result, a large difference in wettability would yield a significant change in evaporation rate. In such a case where there is a significant change in contact angle, and therefore evaporation rate, we expect that the enhanced evaporation rate will shift the evaporation regime upwards. This is because an increase in evaporation rate will produce a thicker film due to mass balance. As a result the transition regime between the evaporation and Landau-Levich regimes will occur at higher speeds. Because of this morphologies of the printed films would then shift to reflect the new balance between the viscous forces from the substrate and a stronger, evaporatively-induced capillary flow. For example, if the transition from twinned to aligned morphologies occurs between 0.5 and 1 mm/s and the evaporation rate is increased due to enhanced wettability, then this transition will shift to higher speeds with twinned morphologies now persisting at 1 mm/s. However, if the wettability is not drastically different, we do not expect any significant change in morphology due to minimally altered evaporation rate. This latter case is what we have seen when printing PII-2T/Chloroform (10 mg/mL) films on OTS-functionalized $SiO_2$ and plasma treated $SiO_2$ (OH-$SiO_2$). We verified surface modification of these substrates by measuring the contact angle of water which was found to be ~108° for OTS-$SiO_2$ and <10° for OH-$SiO_2$ (total wetting). The receding contact angle of our solution on OTS-$SiO_2$ and OH-$SiO_2$ was ~20° and ~15°, respectively. We printed the PII-2T solution over a range of speeds on both of these substrates in order to

compare morphology and thickness. The film thickness vs printing speed is plotted in fig. S15 (right) showing that the measured thicknesses are comparable and that the regimes do not show any significant shift. This is expected as the contact angle of our solution on the two substrates were not significantly different. CPOM images of the printed films are shown in fig. S15 (left) showing that the morphologies are similar at the same printing speed.

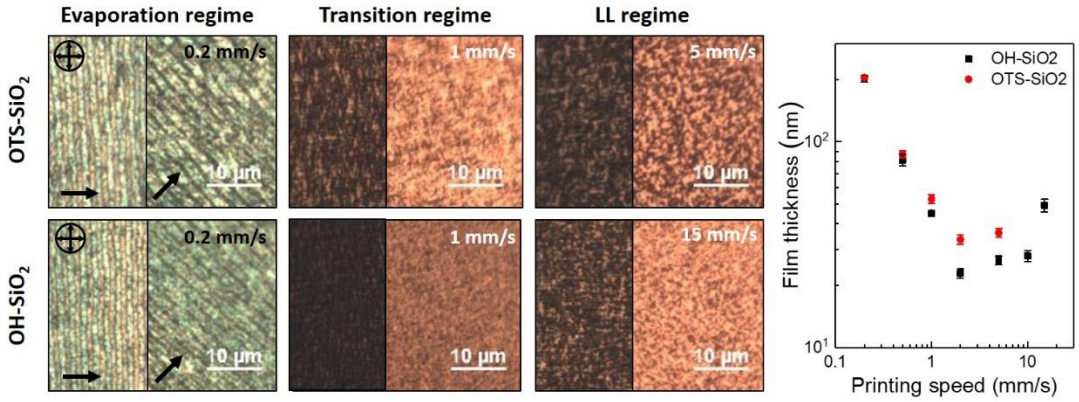


**Fig. S15. CPOM images and thickness of PII-2T films as a function of printing speed using various substrate surfaces.** (Left) CPOM images of the films as a function of printing speed using OTS and plasma-treated $SiO_2$ substrates. The arrows indicate the printing direction. The optical birefringence between the images captured at 0º and 45º provides a qualitative measure of overall chain alignment. The films printed on OH-$SiO_2$ in evaporation regime show clear twinned morphology with birefringence, exhibiting higher intensity when the printing direction is oriented parallel to one of the crossed polarizers. The films printed in transition regime shows a relatively smooth morphology with birefringence but exhibits higher intensity when the printing direction is oriented 45° between the crossed polarizers, indicating high alignment parallel to the printing direction. At 15 mm/s we see that the film still exhibits higher intensity at 45°, however the birefringence is considerably weaker indicating a broader distribution of orientation. These observations are consistent with those formed on OTS-functionalized substrates. (b) Double logarithmic plots of PII-2T film thickness as a function of printing speed for the two substrates. Two regimes, evaporation and Landau-Levich, are clearly identified based on the film thickness and are similar for films printed on both substrates.

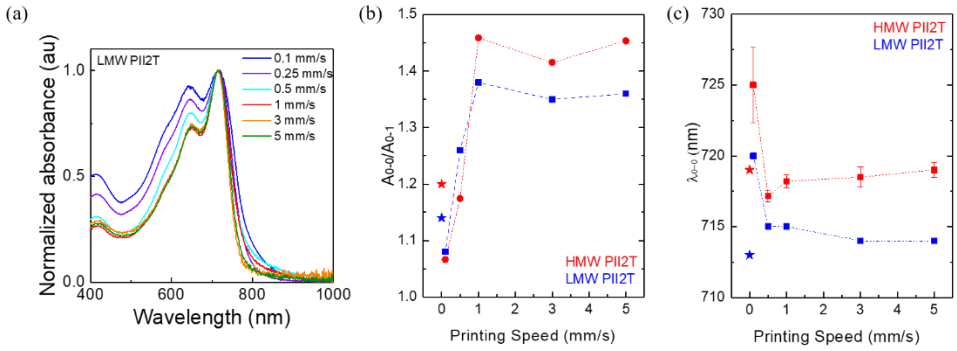


**Fig. S16. UV-vis absorption spectra of low-MW PII-2T films printed at various printing speeds.** (a) Normalized film UV-Vis absorption spectra of LMW PII-2T. The peak broadening decreases with increasing printing speed as was observed for high molecular weight (HMW) PII-2T. (b-c) Comparison of absorption characteristics of LMW (blue color) and HMW (red color) PII-2T films printed at various speeds. The red and blue star marks indicate the peak ratio and position obtained from solution spectra of HMW and LMW PII-2T, respectively. The dashed lines serve as a guide of the trend. The characteristics show a similar trend independent of molecular weight. The relatively lower $A_{0\text{-}0}/A_{0\text{-}1}$ ratio and blue-shifted 0-0 transition for the LMW PII-2T films are obtained which is consistent with our solution spectroscopic study (Section 4.1). This result implies that the flow-induced morphological transition is governed by molecular scale properties (molecular conformation).

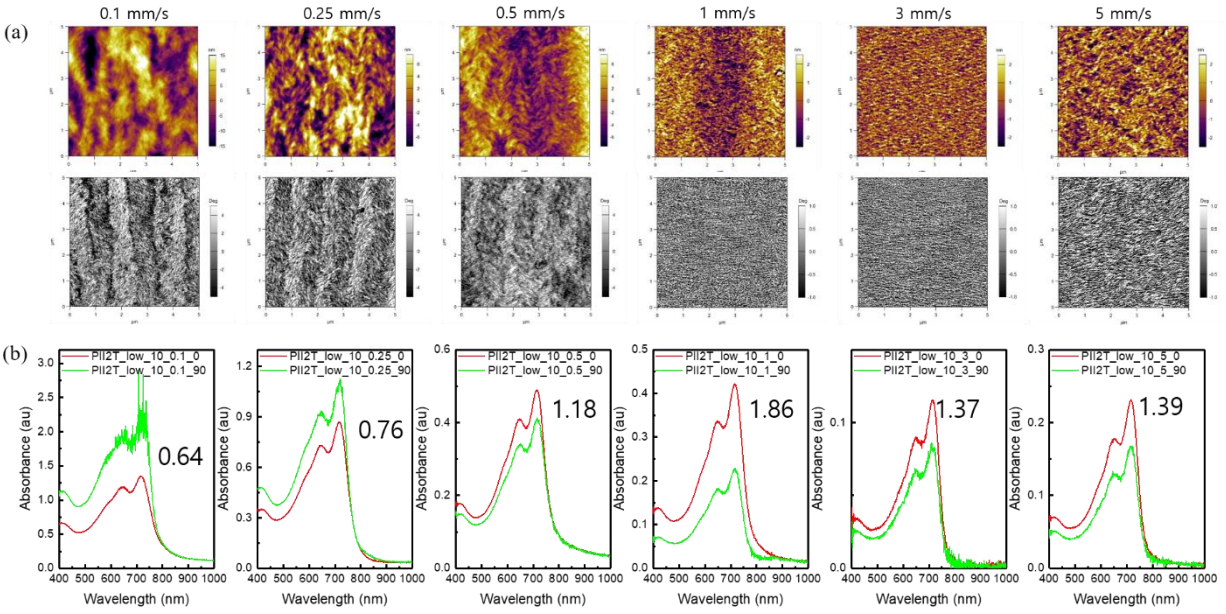


**Fig. S17. Polymer fiber and backbone alignment analysis of low-MW PII-2T films printed at various printing speeds.** (a) AFM height (top) and phase (bottom) images of LMW PII-2T film printed from 0.1−5 mm/s. The images were scanned over 5 x 5 $\mu m^2$. The twinned morphology formed in the evaporation regime (0.1 – 0.25 mm/s) gradually develops into unidirectionally aligned fibers in the transition regime (0.5-3 mm/s). In the Landau-Levich regime (5 mm/s), the fibers are less oriented due to molecular re-orientation prior to

deposition. (b) Polarized UV-Vis absorption spectra and dichroic ratio (insets) of LMW PII-2T films printed at various printing speeds. Polarized absorption spectra of the PII-2T films are shown with the light polarization direction oriented either parallel (red line) or perpendicular (green line) to the printing direction. The degree of alignment of the polymer backbone was characterized using the dichroic ratio $R = A_{\parallel}/A_{\perp}$, with the peak absorbance obtained at ~713 nm. The trend of dichroic ratio change as a function of printing speed shows the alignment transition, identical to what we observed using HMW PII-2T.

**Section S5. Simulation and experimental results of capillary pen writing**

To demonstrate the generality of our experimental and simulation results, we printed films of PII-2T by capillary pen writing using o-dichlorobenzene (o-DCB) as a solvent instead of chloroform. Films were printed at 60°C however the vapor pressure of o-DCB at this temperature is still considerably lower than that of chloroform at 25°C. We use capillary pen writing as an alternative MGP method since it is a useful technique for printing narrow lines and direct-writing arbitrary film patterns (fig. S18a-b). For capillary pen writing the pen was positioned approximately 10 μm from the substrate in order to form a stable meniscus. We noticed during printing that solvent evaporation appeared to be faster compared to blade coating when using the same solvent. This is likely due to the fact that significant evaporation occurs in all directions for pen writing while evaporation occurs mainly on one side at the receding contact line for blade coating since the evaporation at the advancing contact line underneath the blade is diminished. Therefore, the use of a high boiling point solvent was necessary to prevent clogging of the capillary pen and to prevent total evaporation of the small meniscus volume. Additionally, the concentration of the solution was increased to 30 mg/ml in order to produce consistently homogenous films at higher speeds. While MGP methods typically involve planar flows towards the contact line, this is only true for geometries where the height of the meniscus is significantly smaller than its width, such as in blade coating. For capillary pen writing the meniscus is nearly circular with significant

evaporation occurring all around. Therefore, while flow arising from viscous forces may be planar, capillary flow arising from solvent evaporation is not. Despite this, we found our simulations were able to predict film morphologies in the center region of the written lines in a similar manner to blade coated films. This is likely because of the symmetry plane along the centerline where capillary flows in the printing direction are maximum and lateral flows arising from evaporation perpendicular to the printing direction cancel out, leading to flows in this center plane to mimic those in blade coating. Simulations were carried out in a similar fashion to those done for PII-2T/Chloroform blade coating but with changes to material parameters corresponding to the PII-2T/o-DCB solution. To account for the increased evaporation in capillary pen writing, the gas domain height was decreased from the 2 mm used in blade coating to 1 mm, steepening the concentration gradient and effectively increasing evaporative flux. The initial meniscus height was kept at 100 μm, since changing it to 10 μm made very little difference. The initial meniscus curvature was kept the same as for blade coating since increasing it did not significantly affect the regimes and only increased the absolute value of the strain rate. For further discussion on the sensitivity to parameters see Section S1. The predicted and experimentally measured film thicknesses are plotted versus printing speed in fig. S18c, showing good agreement and exhibiting the three printing regimes. The velocity profile and strain rate are shown for representative speeds in each regime in fig. S18d while the full speed series can be seen in fig. S19. As expected we observed the same transitions in meniscus shape and flow profile as when blade coating with chloroform but at lower speeds due to the lower vapor pressure of o-DCB. Figure S20 summarizes the evolution of strain rate and residence time in the meniscus for all speeds, with rapidly rising strain rate and finite residence again occurring in the transition regime. Representative CPOM (the full speed series shown in fig. S21) and AFM images of the printed films are shown in fig. S18e, displaying characteristic changes in birefringence and

morphology with the printing regimes. As in the previous case, the twinned domains transition towards a unidirectionally aligned film along the printing direction with increasing speed. Additionally, we observe a concomitant birefringence flip during this transition. The AFM images clearly show the less aligned fibers that form twinned domains at low speeds (0.05 mm/s) progress into straight, parallel fibers at higher speeds in the transition regime (>0.1 mm/s). Again, the formation of aligned fibers parallel to the printing direction occurs when the strain rate begins to rise while residence time remains relatively short and finite.

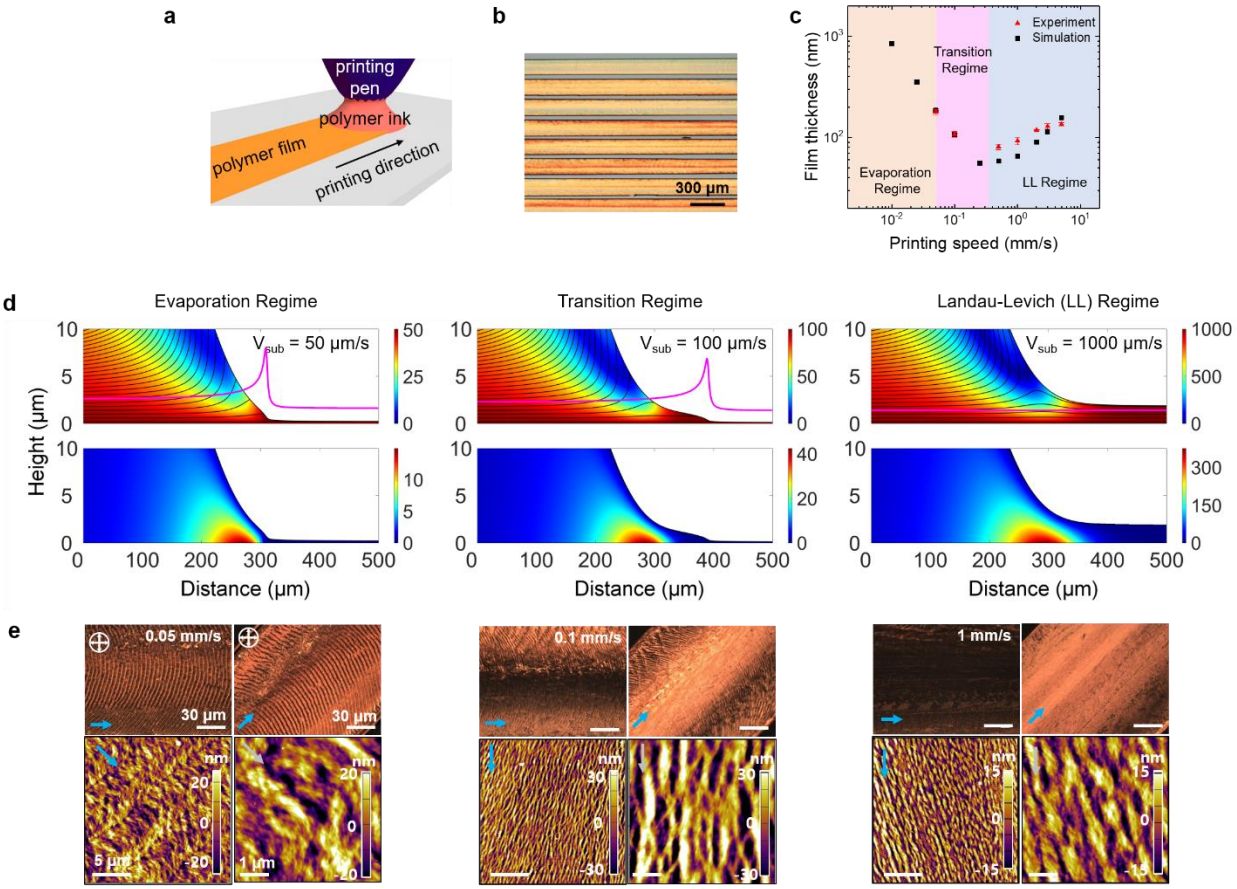


**Fig. S18. Flow-induced morphological transition for pen-written PII-2T films and velocity and strain rate from computational fluid dynamics simulations.** (a) Schematic of capillary pen writing process to print PII-2T films using PII-2T/o-DCB ink solution. (b) Optical microscopy image of PII-2T line array printed by capillary pen writing. (c) Comparison between experimentally measured film thickness (red triangles) and predicted film thickness from simulation (black squares) as a function of printing speed. Evaporation, Transition, and Landau-Levich regimes are shown. (d) (Top) velocity magnitude and streamlines for corresponding printing speeds of the three regimes. Evaporative flux profile is overlaid (magenta line) showing peak evaporation occurring at the contact line for the evaporation and transition regimes. (Bottom) Strain rate in the meniscus for corresponding printing speeds of the three regimes. (e) (Top) CPOM images of pen-written PII-2T films are shown oriented at 0° and 45° relative to cross polarizers for each representative speed of the three regimes. The arrows indicate the printing direction and the crossed arrows indicate the orientation of the crossed polarizers. The printing speed of each image are denoted in the upper right corner. (Bottom, left) 20 x 20 $\mu m^2$ and (bottom, right) 5 x 5 $\mu m^2$ scanned AFM height images of PII-2T films for the three regimes.

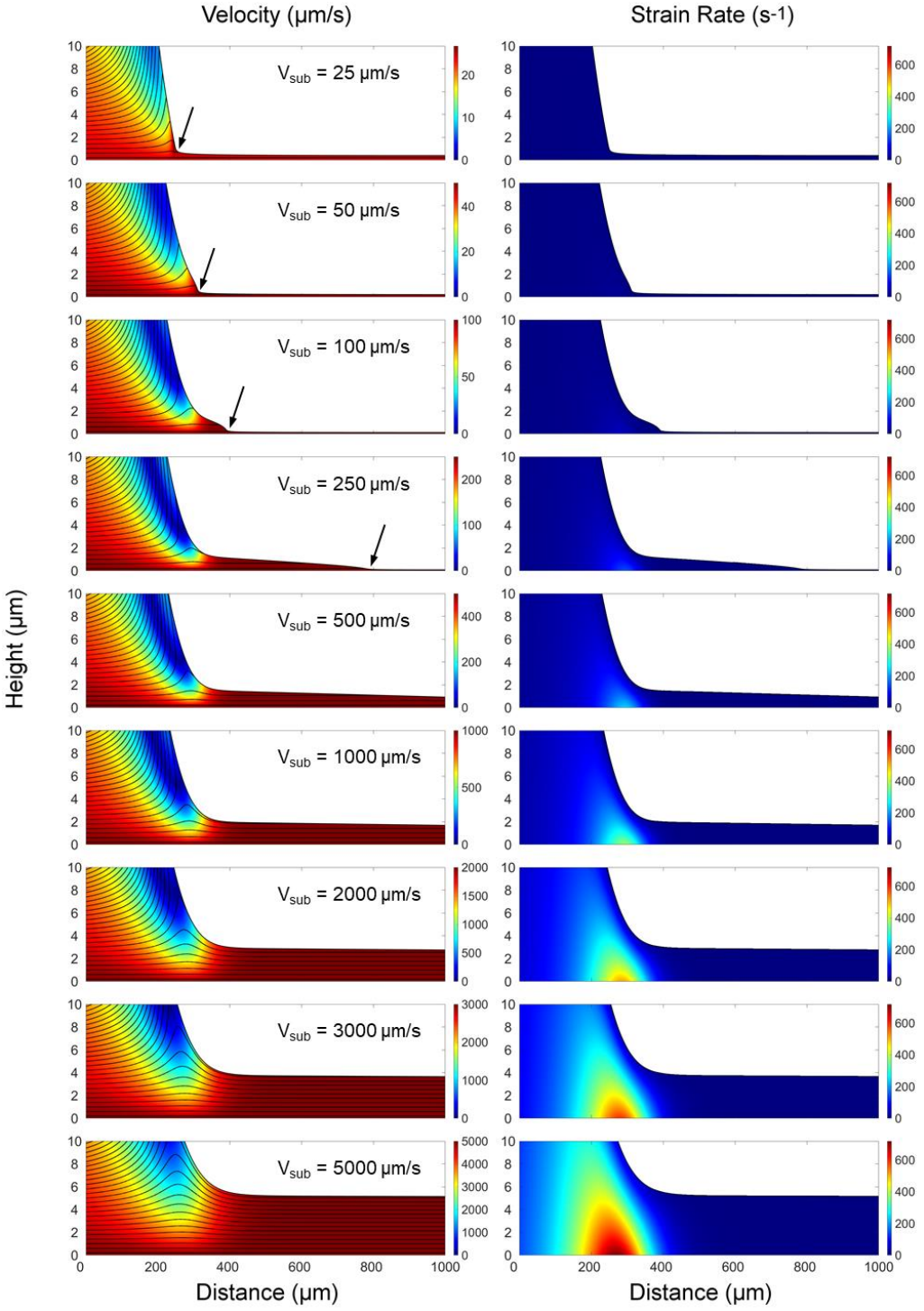


**Fig. S19. Complete speed series of velocity fields and strain rates for PII-2T/o-DCB blade coating simulations.** (left) Velocity magnitude and streamlines for all printing speeds. The meniscus contact line is noted by black arrows. (right) Strain rate for all printing speeds. Color bar for all speeds ranges from 0 $s^{-1}$ to 718.7 $s^{-1}$, the maximum strain rate for 5000 μm/s.

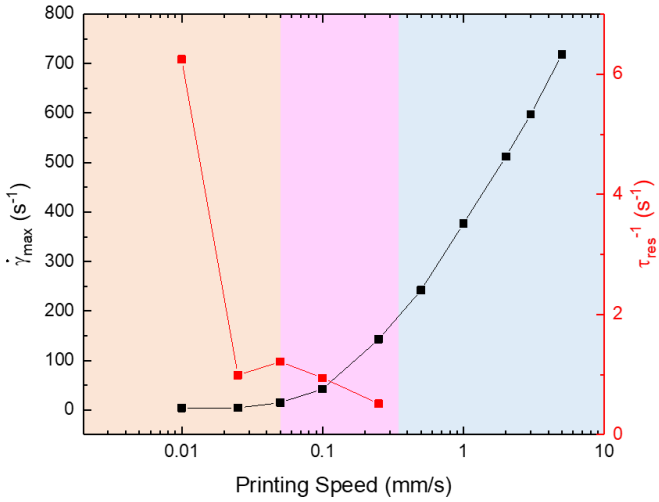


**Fig. S20. Maximum strain rate and inverse residence time as a function of printing speed for PII-2T/o-DCB simulations.** Strain rate (black) remains constant in the evaporation regime then begins to increase drastically in the transition regime due to increasing viscous forces. Residence time (red) from position of maximum strain rate to the contact line is initially short in the evaporation regime and increases with increasing speed. Residence time remains relative short and finite in the transition regime then approaches infinity in the Landau-Levich regime allowing polymer conformation to relax.

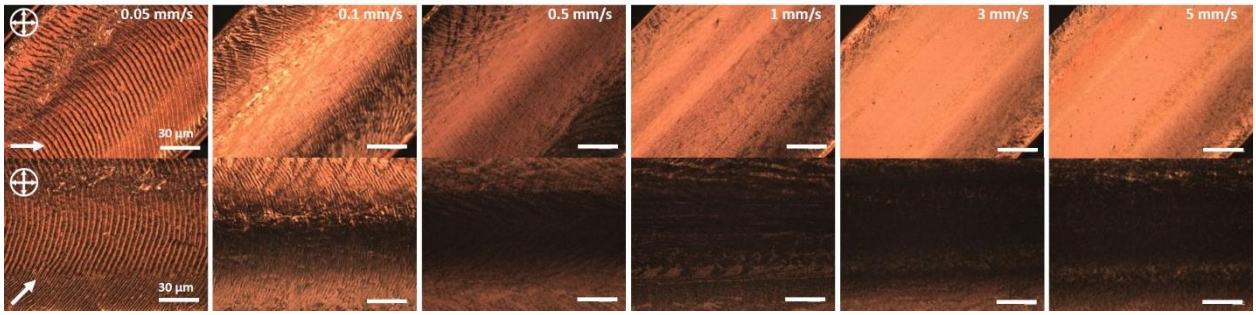


**Fig. S21. CPOM images of the capillary pen–written films as a function of printing speed.** The CPOM images are of films with the printing direction oriented 0° and 45° with respect to the polarizer axis. The arrows denote the printing direction, and the crossed arrows indicate the orientation of the crossed polarizers. The printing speed is denoted in the upper right corner. All scale bars are 30 µm. It is clear that between 0.05 mm/s and 0.1 mm/s we see that the center of the film begins to undergo a morphological transition from twinned to aligned domains as evidenced by the emerging birefringence throughout the entire central region. With increasing speed, we see that this central birefringent region becomes wider until about 1 mm/s in the Landau-Levich regime. At the highest speeds probed here, we do not see fibers begin to lose alignment yet and attempts to print at further higher speeds yielded less uniform films. This may be due to the reduced height and increased curvature of the meniscus in capillary pen writing which results in higher strain rates and lower residence times when compared to blade coating at similar conditions.

In order to compare results with blade coating, we printed films with the exact same conditions as capillary pen writing using o-DCB as the solvent. Representative CPOM and AFM images of the PII-2T/o-DCB blade coated films are shown in fig. S22. The blade coated o-DCB samples display morphological transitions at similar printing speeds as the pen-written films. This is in line with the fact that our simulations more closely match blade coating but can still be used to describe capillary pen writing near the central symmetry plane.

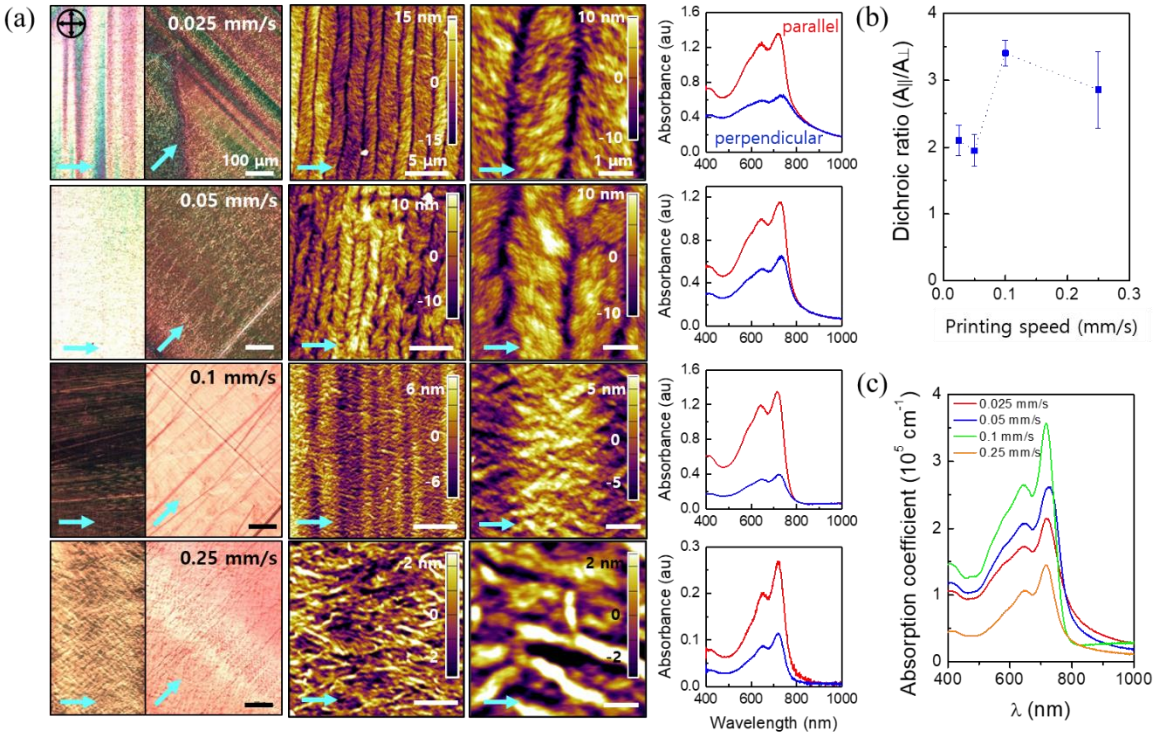


**Fig. S22. Flow-induced morphological transition in PII-2T films printed using o-DCB solvent.** (a) CPOM images of the films as a function of printing speed. CPOM images are of films with the printing direction oriented 0° and 45° with respect to the polarizer axis. The PII-2T films were printed with 30 mg/ml o-DCB solution. The arrows denote the printing direction, and the crossed arrows indicate the orientation of the crossed polarizers. The printing speed is denoted in the upper right corner. The scale bars are 100 μm (CPOM), 5 μm (middle AFM) and 1 μm (right AFM). The birefringence difference and morphology transition are clearly observed in the transition regime starting between 0.05 and 0.1 mm/s. It is noted that the crystalline domain size is approximately three-fold larger than those produced with chloroform solution. Polarized UV-Vis absorption spectra of PII-2T films are measured with the light polarization direction oriented either parallel (red line) or perpendicular (blue line) to the printing direction. (b) Dichroic ratio ($R = A_{\parallel}/A_{\perp}$) of PII-2T films printed at various printing speeds. An apparent orientation flipping of polymer backbone is not observed probably because the aligned polymer fibers in the large crystalline domain of the films printed in evaporation regime have relatively small angles with respect to

the printing direction. Still, the degree of alignment along the printing direction increased at the transition regime. (c) Absorption coefficient of the films printed at various printing speeds. The highest coefficient is observed for the PII-2T film printed at the transition regime.

## Section S6. Characterization of molecular orientation and packing structures

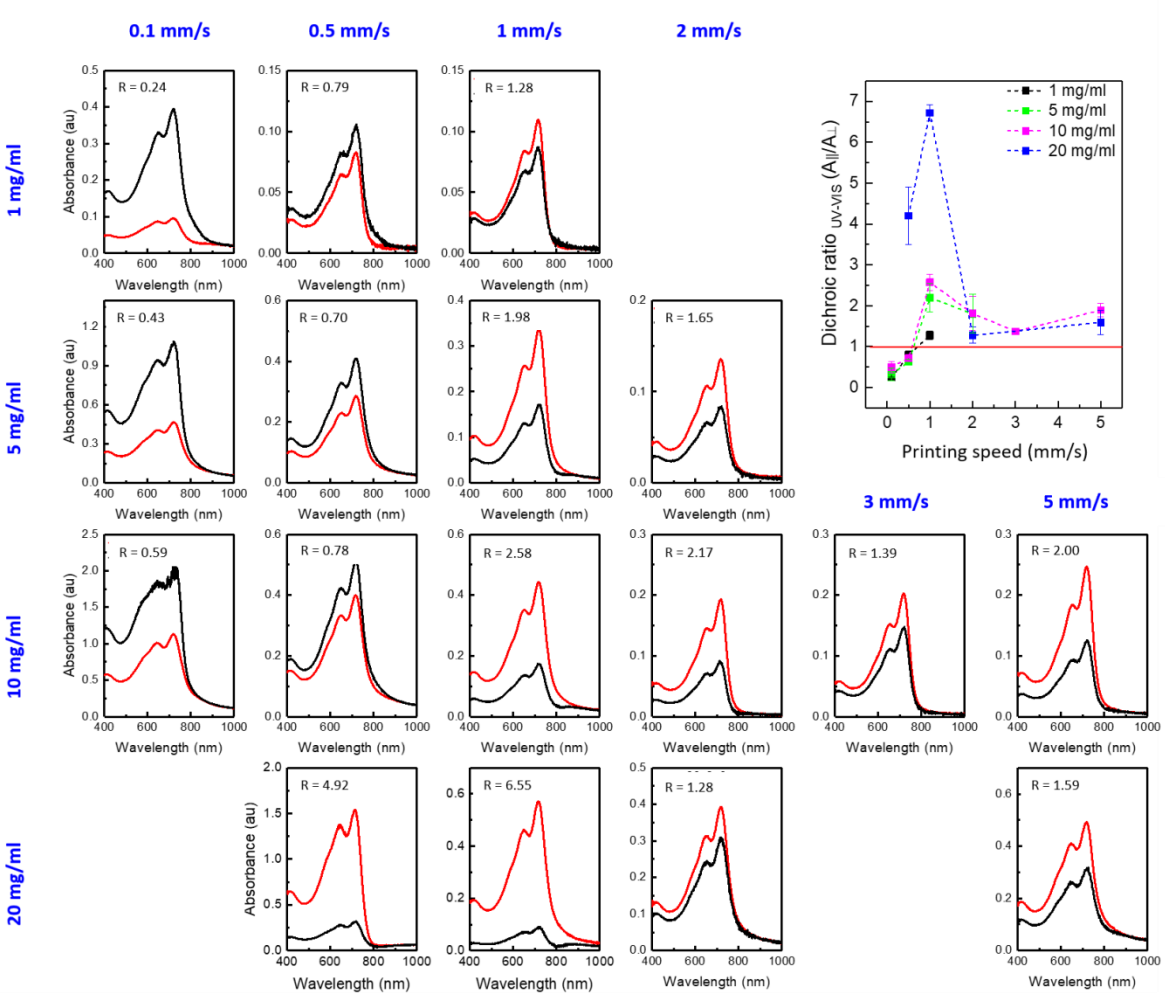


**Fig. S23. Polarized UV-vis absorption spectra and dichroic ratio of PII-2T films printed at various printing speeds with different concentration solutions.** Polarized absorption spectra of the PII-2T films are shown with the light polarization direction oriented either parallel (red line) or perpendicular (black line) to the printing direction. The degree of alignment of the polymer backbone was characterized using the dichroic ratio $R = A_{\parallel}/A_{\perp}$, with the peak absorbance obtained at ~719 nm. Regardless of solution concentration, the printing speed-dependent dichroic ratio shows the alignment transition between 0.5 and 1 mm/s where strain rate rises rapidly. It is noted that the degree of alignment increased in transition regime for the high viscosity solution (20 mg/ml) although the apparent polymer backbone orientation was not flipped. This result is probably attributed to the high entanglement of polymer chains in the high viscous solution which can be aligned with the flow direction with even lower strain rate.

GIXD data analysis was performed using the GIXSGUI software which includes a correction for the polarization of the synchrotron X-ray beam (47). The π–π stacking anisotropy was calculated by extracting the intensity of the edge-on π–π stacking peak from both parallel and perpendicular scans. The edge-on π–π stacking peaks were obtained from a sector cut of $-88° < \chi < -83°$ at $q_y$ = 1.75 Å. Partial pole figures (shown in Fig. 3E of the main text) were constructed by extracting the (010) π–π stacking peak intensities as a function of the polar angle, χ (13−88° binned into 5° increments) to analyze out-of-plane ordering distribution (*17*). Multipeak fitting was performed with Igor Pro to deconvolute the π–π stacking peak from the amorphous ring, $SiO_2$ scattering and the crystalline OTS peak. The π–π stacking peak was fitted with a Gaussian function to obtain the peak position, peak area and full width half-maximum (FWHM). The peak area was further normalized by the film thickness and beam irradiated area on the films to allow comparison across samples.

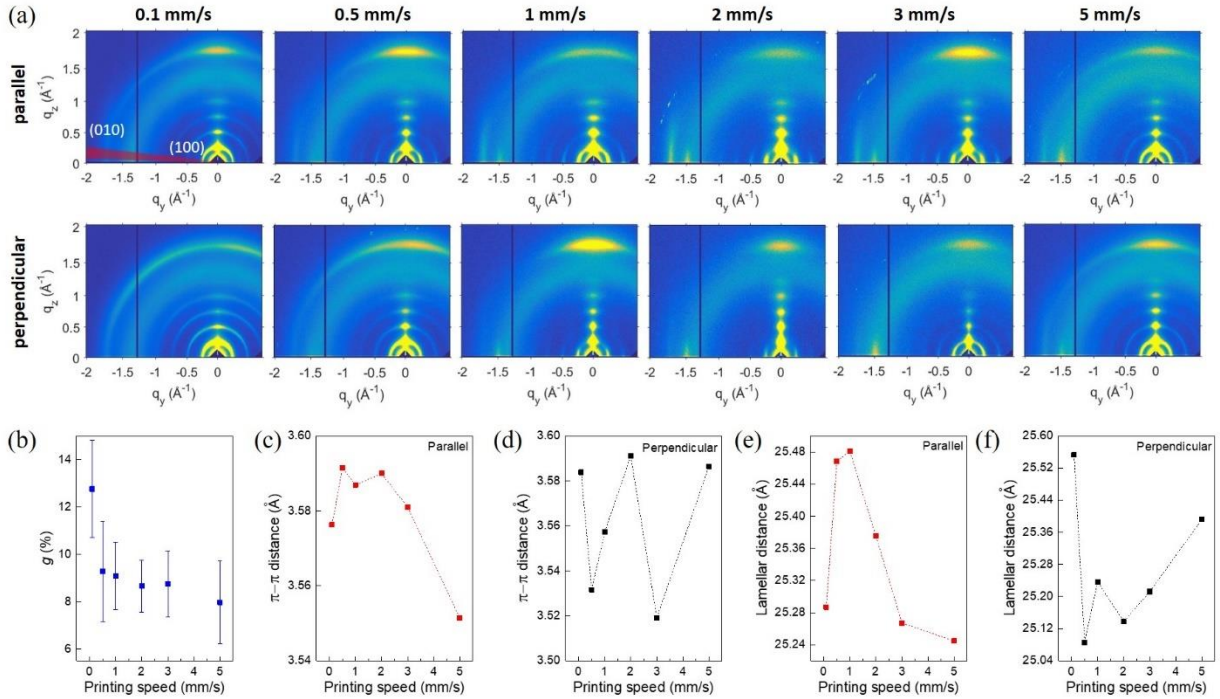


**Fig. S24. Comparison and analysis of 2D x-ray diffraction patterns.** (a) 2D X-ray scattering pattern comparison of printing speed dependent films with the incident beam oriented parallel and perpendicular to the printing direction. The PII-2T films were printed with 10 mg/ml chloroform solutions. The red colored area indicates a sector cut of $-88° < \chi < -83°$ to analyze in-plane alignment anisotropy of edge-on π–π stacking. (b-f) GIXD peak analysis performed on the films from parallel and perpendicular measurements as a function of printing speed (b) Paracrystalline disorder (g-factor) along the π-stacking direction (010), obtained by the center position ($q_y$) and FWHM of diffraction peaks (48). (c, d) Edge-on π-π stacking distance obtained from (010) peak at $q_y \approx 1.75$ Å for each parallel and perpendicular measurement. (e, f) Lamellar stacking distance obtained from (100) peak at $q_y \approx 0.25$ Å for each parallel and perpendicular measurement.

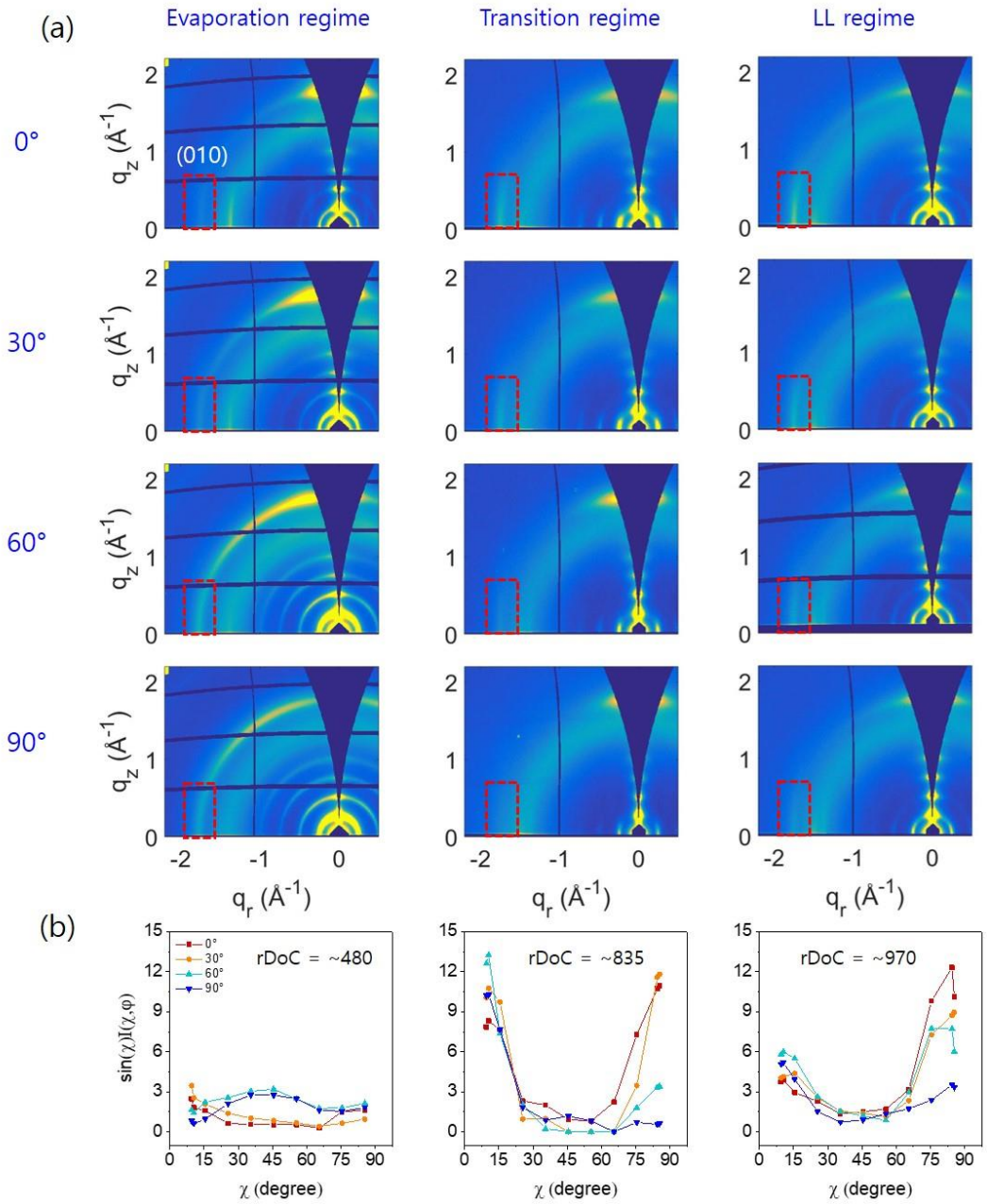


**Fig. S25. GIXD analysis of PII-2T films obtained at multiple in-plane rotation angles.** (a) GIXD scattering patterns of polymer films printed in three regimes. 2D X-ray diffraction patterns of the films are compared with the incident beam oriented at φ = 0° (parallel), 30°, 60°, and 90° (perpendicular) with respect to the printing direction. The red dashed boxes mark edge-on π–π stacking (010) peaks. (b) Geometrically corrected intensity of the (010) peak is shown for the three films as a function of polar angle χ and φ; polar angle χ denotes the out-of-plane orientation of the π-stacks, with χ = 0 and 90° representing "edge-on" and "face-on" orientation with respect to the substrate plane, respectively. Increasing printing speeds re-orients the crystalline domains towards more 'face-on' and 'edge-on' orientations (less isotropic out-of-plane) with significantly altering the crystallinity of the thin films. The rDoC was calculated by integrating the geometrically corrected peak intensities over χ (from 7° to 88°) and the flow-induced aligned films improved the rDoC by ~75% from the evaporation to the transition regime.

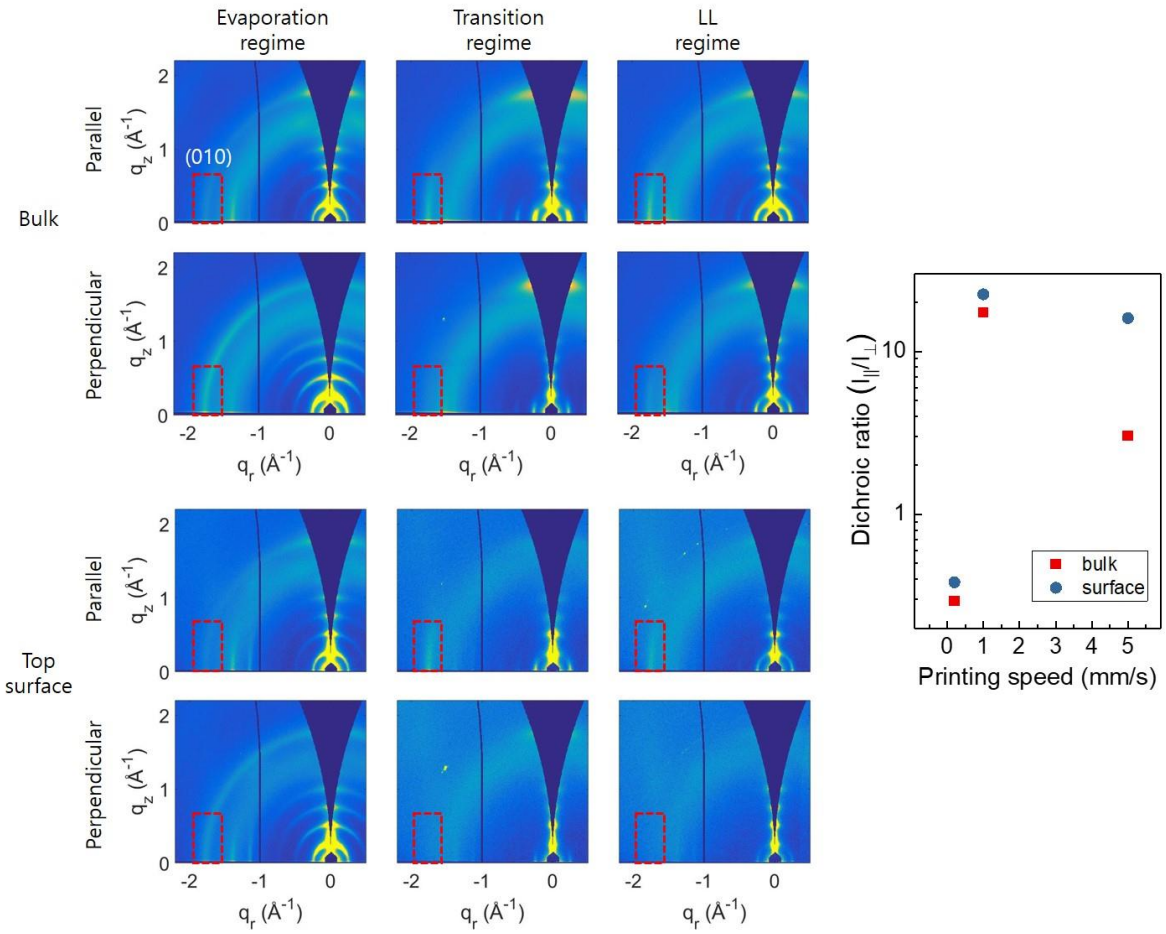


**Fig. S26. GIXD characterization of PII-2T morphology in the bulk and top surfaces of printed films.** (Left) 2D X-ray scattering patterns from both bulk and surface measurements of printed films with the incident beam oriented parallel and perpendicular to the printing direction. The PII-2T films were printed with 10 mg/ml chloroform solutions. The red boxes indicate edge-on π–π stacking peaks used to analyze in-plane alignment anisotropy. The scattering patterns reveals a similar morphology outcome that the crystallites at the top surface oriented same as those in the film. (Right) In-plane π-π stacking alignment anisotropy comparison of the films as a function of printing speed for bulk and surface of the films. The dichroic ratio of $R = I_{\parallel}/I_{\perp}$ was used to quantify the degree of in-plane alignment, where $I_{\parallel}$ and $I_{\perp}$ are the normalized edge-on π–π stacking integrated peak area with the incident beam parallel and perpendicular to the printing direction, respectively. The highest R value is observed from the films printed in the transition regime for both bulk and surface of the films.

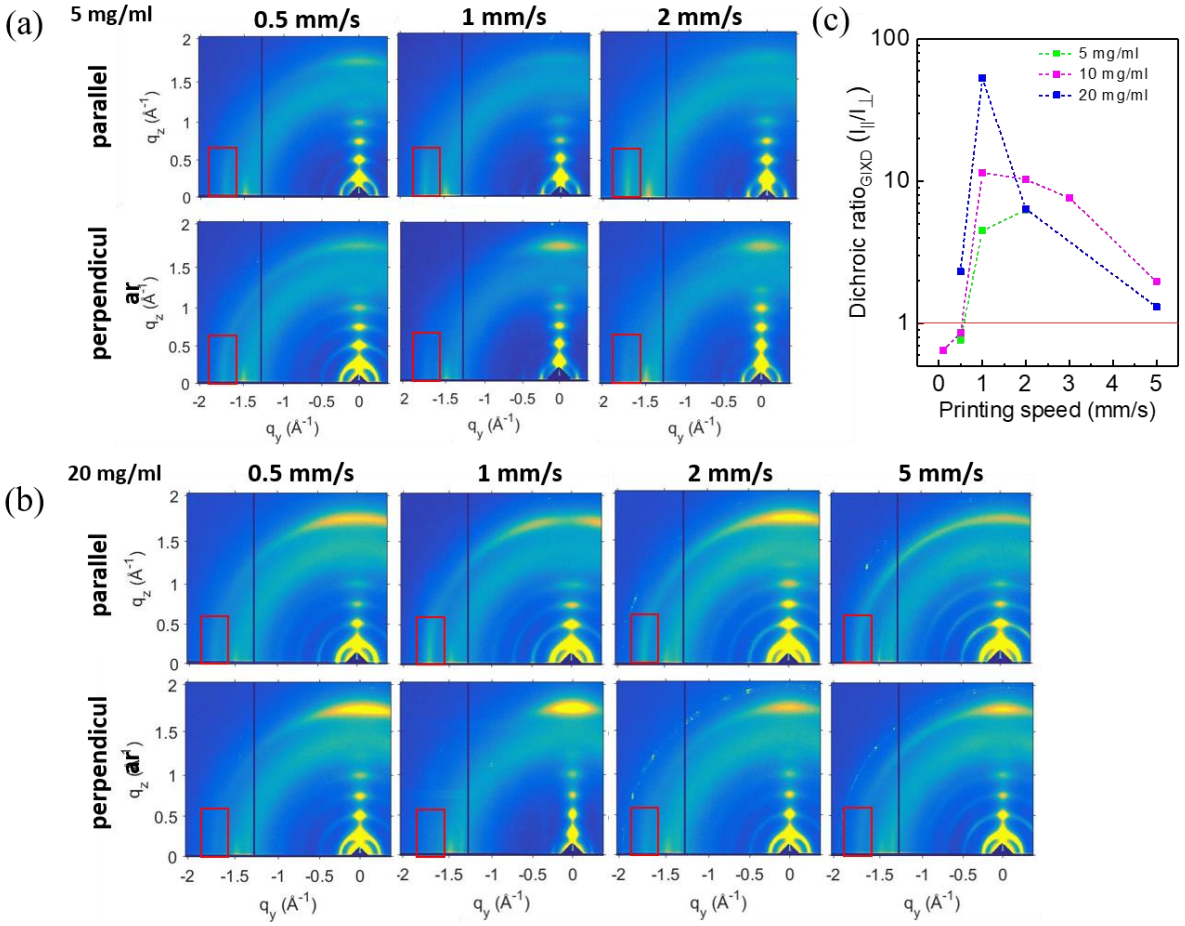


**Fig. S27. GIXD characterization of PII-2T films printed at various printing speeds with different solution concentrations.** (a, b) 2D X-ray scattering pattern comparison of printed films with the incident beam oriented parallel and perpendicular to the printing direction. The PII-2T films were printed with 5 or 20 mg/ml chloroform solutions. The red boxes indicate edge-on π–π stacking peaks used to analyze in-plane alignment anisotropy. (c) In-plane π-π stacking alignment anisotropy comparison of the films as a function of printing speed depending on solution concentration. The dichroic ratio of $R = I_{||}/I_{\perp}$ was used to quantify the degree of in-plane alignment, where $I_{||}$ and $I_{\perp}$ are the normalized edge-on π–π stacking integrated peak area with the incident beam parallel and perpendicular to the printing direction, respectively. The highest R value is observed from the films printed in the transition regime for all solution concentrations.

## Section S7. Fabrication and measurement of devices

Top-contact and bottom-gate field-effect transistor (FET) devices were fabricated on the PII-2T printed films. A heavily doped n-type $Si/SiO_2$ wafer was used as the substrate, with the conductive Si and $SiO_2$ surface layer (300 nm) functioning as the common gate electrode and gate dielectric, respectively. The $SiO_2$ substrate surface was first modified with a self-

assembled crystalline OTS monolayer to reduce surface charge traps as done previously (49). Then, the films were printed on the OTS-functionalized $SiO_2$ surface by meniscus guided coating to form the active channel layers. Finally, source–drain (S–D) electrodes were deposited onto the PII-2T films by evaporation of $MoO_3$ (8 nm) and subsequently Ag (70 nm) using a shadow mask. The channel width and length were 26 μm and 360 μm, respectively. Thermal annealing treatment at 200 °C under a nitrogen environment was carried out to enhance crystallinity and improve the charge transport. All electrical measurements were performed in a nitrogen environment using a Keysight B1500A semiconductor parameter analyzer. The field-effect mobility (μ) and threshold voltage ($V_{th}$) were calculated in the saturation regime ($V_{DS}$ = −100 V) by plotting the square root of the drain current versus the gate voltage using $I_{DS} = (WC_i/2L)\mu(V_{GS}-V_{th})^2$, where $I_{DS}$ is the source-drain current, $C_i$ is the capacitance of the dielectric (11 nF $cm^{-2}$ for OTS-treated 300 nm $SiO_2$ layer), $V_{GS}$ is the gate voltage, and W and L are the channel width and length, respectively. Average data were obtained from the analysis of more than 5 independent devices.

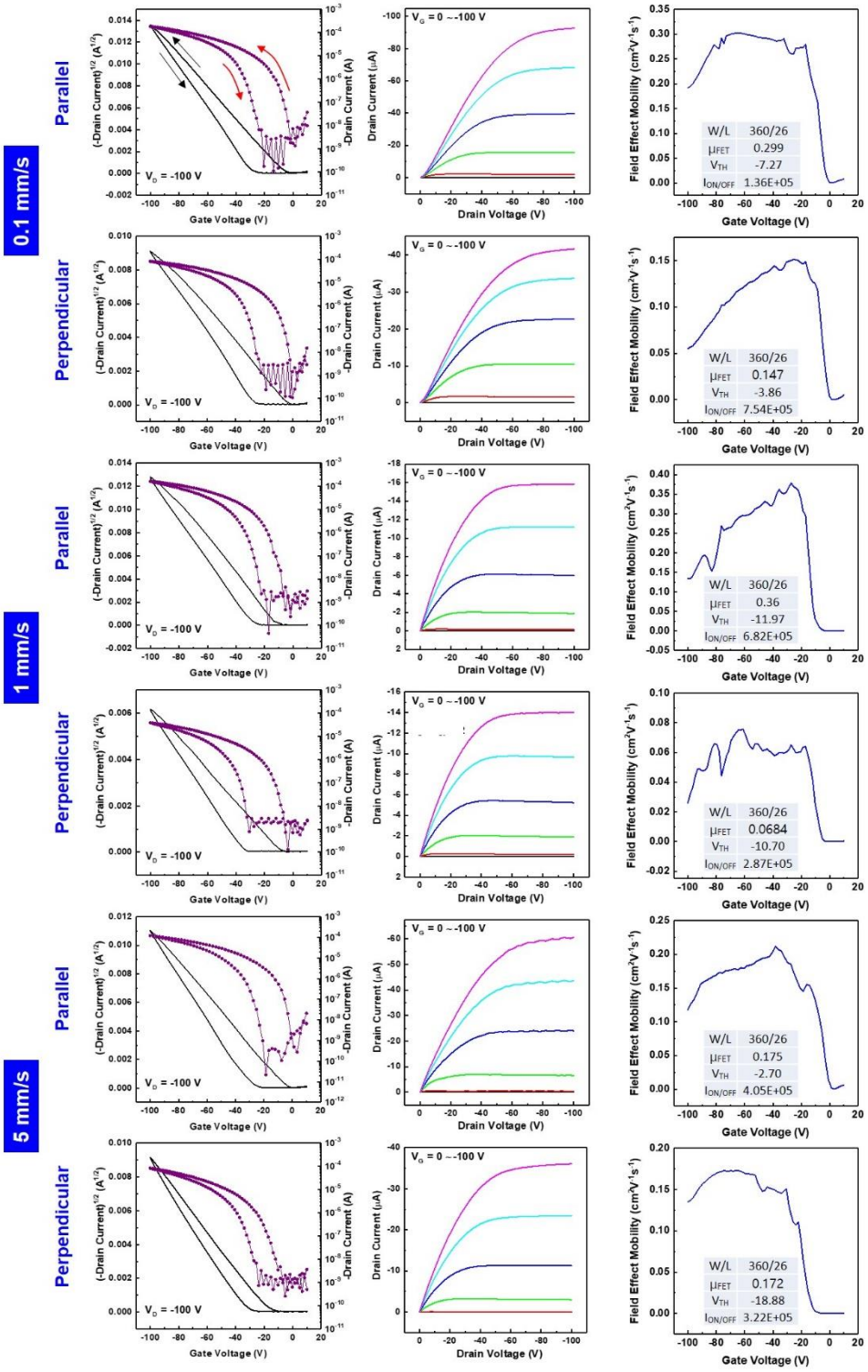


**Fig. S28. Electrical characteristics for as-prepared PII-2T devices without post-thermal treatment.** Double-sweep transfer characteristics of the PII-2T FET devices in log scale (purple line with dots) and linear scale (black line) at $V_{DS}$= −100 V. The curves were obtained from measurements parallel and perpendicular to the printing direction. The arrows indicate the direction of $V_{GS}$ sweep. The large hysteresis between forward and backward sweeps may be caused by the large bias stress, contact resistance, or low capacitance of the

$SiO_2$ dielectric layer. The device mobility was extracted from a slope of the forward sweep in linear scale. The corresponding output characteristics show clear saturation regime at $V_{DS}$ = −100 V. The contact resistance is nearly negligible for both 1 and 5 mm/s-printed films due to the efficient hole carrier transport arising from the inclusion of a $MoO_3$ layer in the Ag electrode (Ag: 4.6eV vs $MoO_3$-Ag: 5.4 eV) (50). In contrast, the contact resistance for 0.1 mm/s-printed film FETs may be attributed to charge traps at the interface due to the large surface roughness. Gate-voltage dependent mobility shows nearly saturation behavior at $|V_G|$ > 30 V. Device properties are denoted in the insets of all gate-voltage dependent mobility plots. The mobility anisotropy was observed for the films produced in transition regime (1 mm/s), increasing by up to fivefold when measured parallel (along polymer backbone) with respect to the printing direction rather than perpendicular.

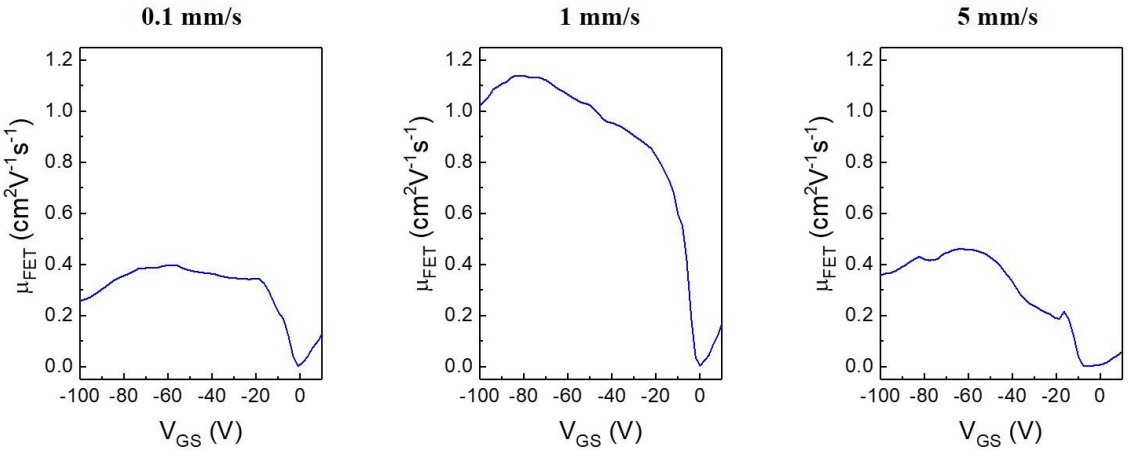


**Fig. S29. Gate voltage–dependent mobility as a function of gate bias, extracted from the transfer curves shown in Fig. 4B.**

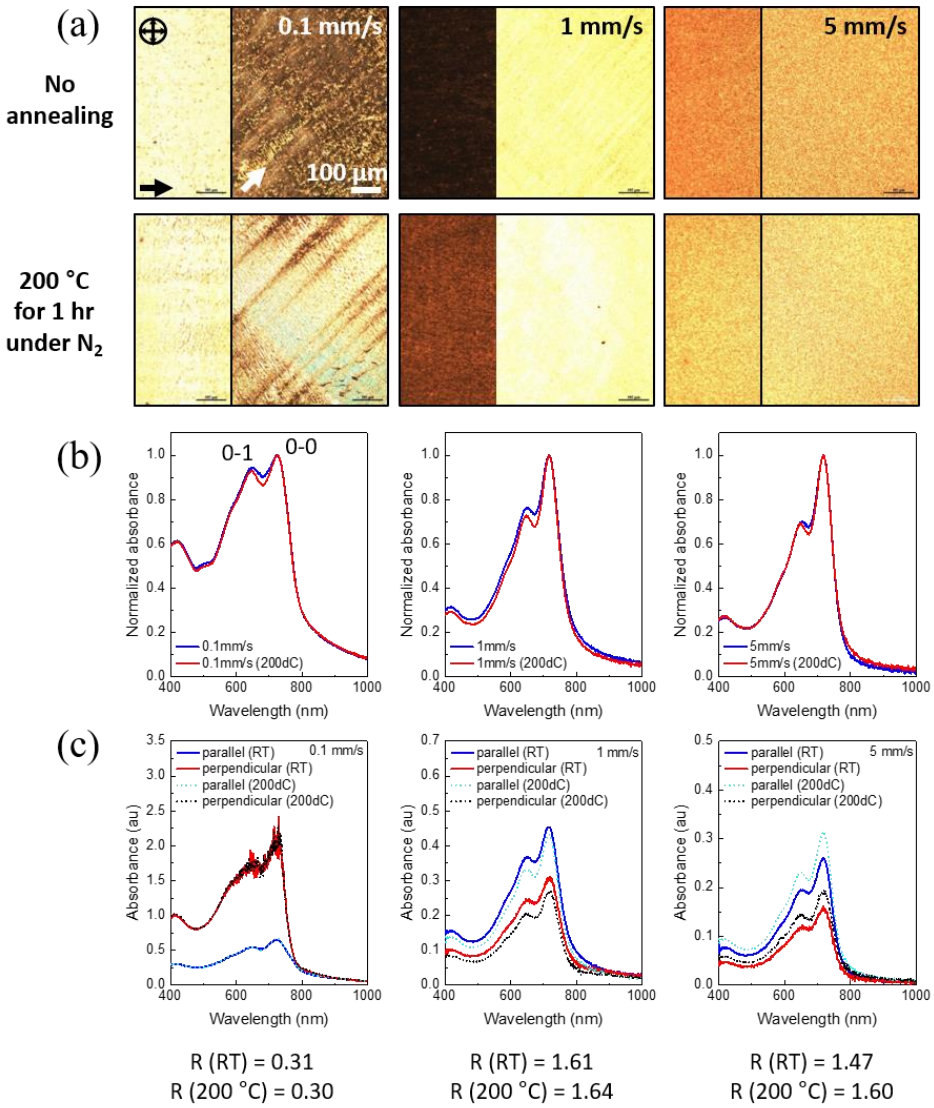


**Fig. S30. Thermal annealing effect of printed PII-2T films.** (a) CPOM images of the as-prepared and thermal annealed PII-2T films as a function of printing speed. The CPOM images correspond to films printed with the printing direction oriented 0° and 45° with respect to the polarizer axis. The arrows indicate the printing direction, and the crossed arrows indicate the orientation of the crossed polarizers. The printing speed is denoted in the upper right corner. All scale bars are 100 μm. The overall birefringence is enhanced after thermal annealing of all the films, which may be attributed to an increased size of crystalline domains and/or improved packing of polymer molecules. (b) Normalized UV-Vis absorption spectra of as-prepared and thermal annealed PII-2T films. After annealing the films at 200 °C, the PII-2T films show barely any change in peak shift or absorption intensity ratio $A_{0-0}/A_{0-1}$, suggesting that the packing conformation of the PII-2T did not change. (c) Polarized absorption spectra of as-prepared and thermal annealed PII-2T films. The dichroic ratio ($R = A_{\parallel}/A_{\perp}$) of each film before and after thermal annealing is shown at the bottom of each graph. The values were not significantly different before and after annealing which suggests that annealing the films did not lead to a further change in the degree of polymer alignment. Thus, we believe that the enhanced field-effect mobility of thermal annealed films is caused by increased crystalline domain size.

## Section S8. Understanding the molecular origin of flow-induced morphological transition by comparing polymer structures

All calculations in this study were carried out using the same hybrid functional and basis set, as implemented in the Gaussian 16 package. The dimers of PII-2T and PTII-2T are fully relaxed at the DFT level, as shown in the main text (Fig. 5A). Torsional potential energy surfaces (PESs) provide key information for molecular thermodynamic state functions. Figure S31 reports the PES along two relevant degrees of freedom, namely the twisting around the intra-acceptor double bond and the rotation around the donor-acceptor single bond. While the intra-acceptor torsion potential features a steep profile centered around a fully planar conformation in the case of the thiophene-based TIIG acceptor unit, there is a significant departure away from planarity when replacing the thiophene by benzene moieties in IIG (likely resulting from the larger steric hindrance with the oxygen of the amide group, but also differences in aromaticity). Likewise, a shallow minimum with an out-of-plane ~30° rotation angle is predicted in PII-2T, against a planar backbone in PTII-2T. As these calculations are performed on isolated polymer chains, they ignore important side-chain effects in the solid, so should be considered from a qualitative point of view only. With this caveat, we conclude that compared to PTII-2T that adopts a rather rigid and planar equilibrium conformation, PII-2T with its soft potential centered around a twisted structure should be more sensitive to changes in flow.

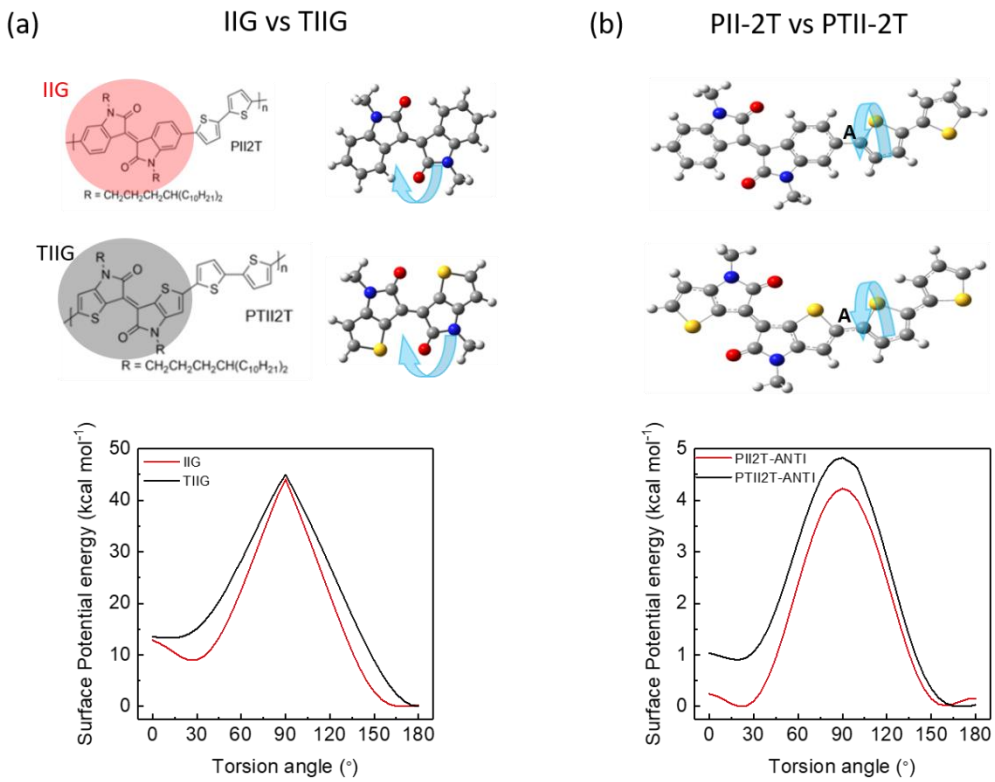


**Fig. S31. Calculated torsion potentials of PII-2T and PTII-2T.** (a) Molecular structures of PII-2T and PTII-2T (top) and the potentials for intra-torsion of acceptor units (bottom). (b) Molecular structures of PII-2T and PTII-2T showing rotation between acceptor and donor units (top) and the potentials between them.

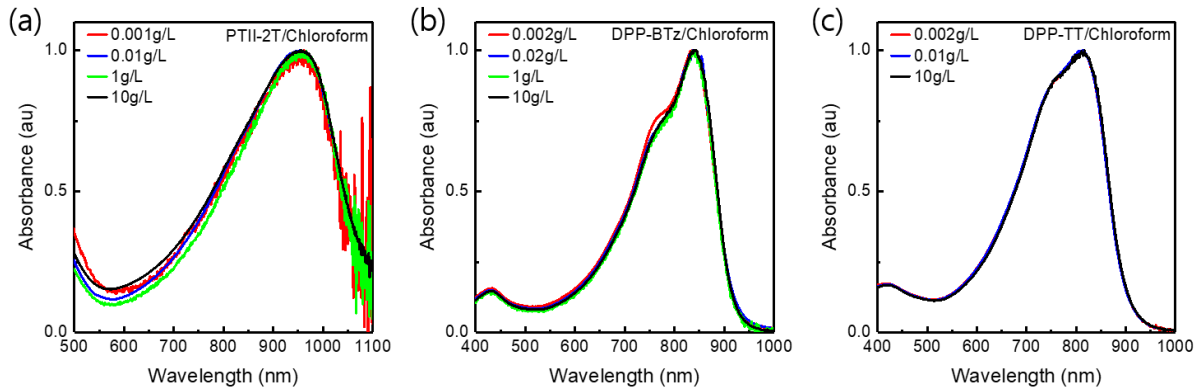


**Fig. S32. Normalized solution UV-vis absorption spectra of PTII-2T, DPP-BTz, and DPP2T-TT prepared in chloroform with various concentrations from 0.001 to 10 g/liter.** Because there is no significant aggregation in solutions, the change in absorption coefficient with printing speed is more likely caused by conformation differences.

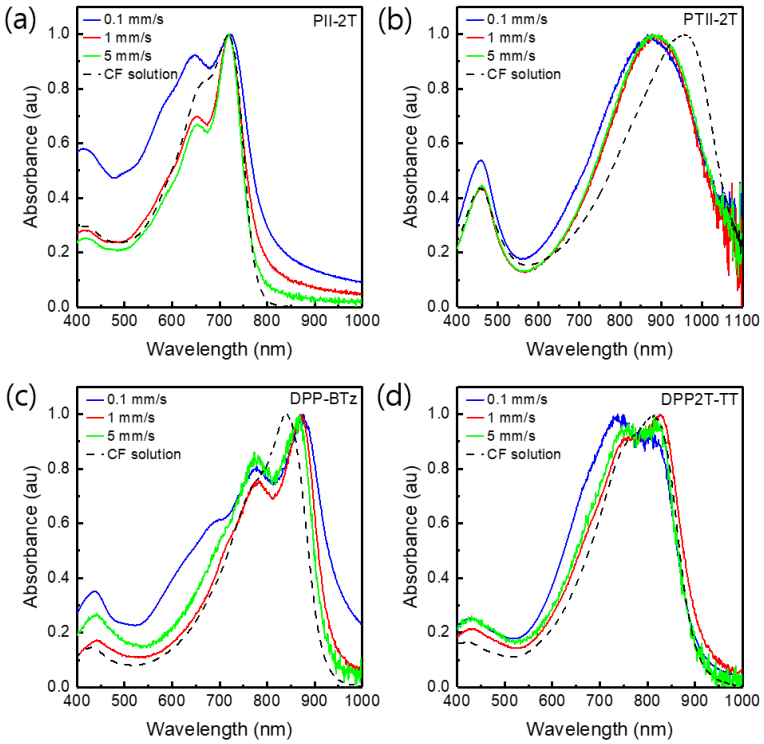


**Fig. S33. Solution and film UV-vis absorption spectra of PII-2T, PTII-2T, DPP-BTz, and DPP2T-TT.** Normalized UV-Vis absorption spectra of solution (black dash line) and films for PII-2T (a), PTII-2T (b), DPP-BTz (c) and DPP2T-TT (d).

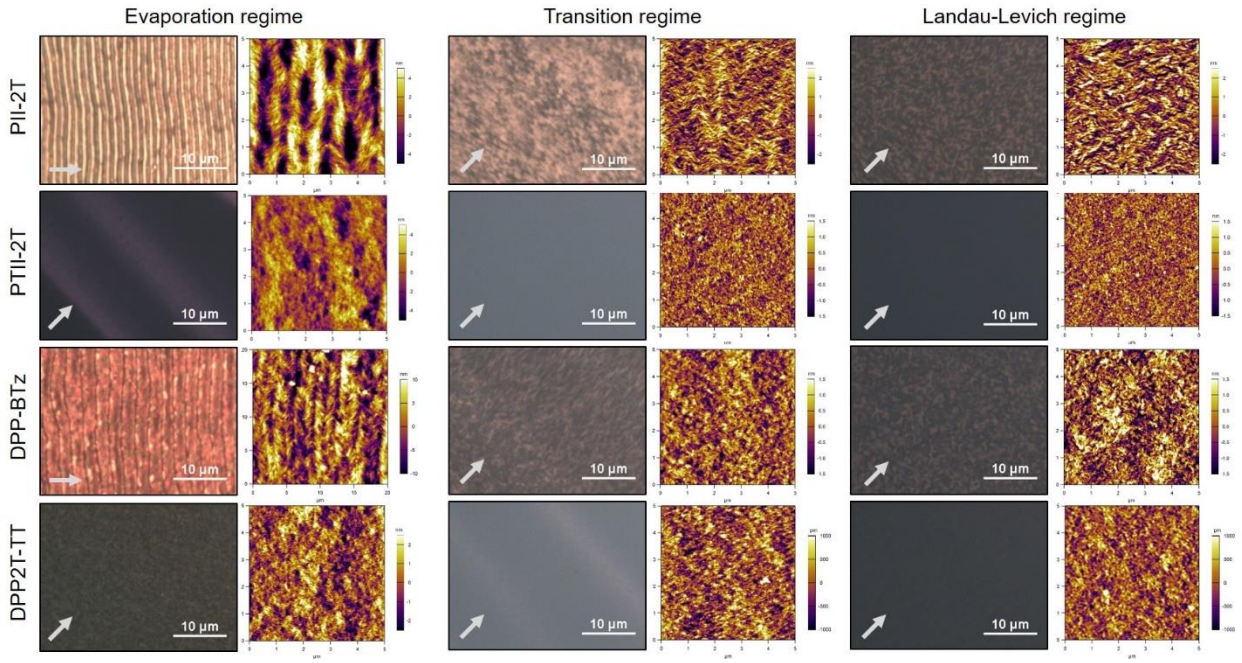


**Fig. S34. Morphology characterization of PII-2T, PTII-2T, DPP-BTz, and DPP2T-TT polymer films prepared in each regime.** The CPOM images of films with the printing direction oriented 0° and 45° with respect to the polarizer axis. The arrows denote the printing direction, and the crossed arrows indicate the orientation of the crossed polarizers. The AFM images were scanned over 5 x 5 $\mu m^2$ except the DPP-BTz (20 x 20 $\mu m^2$) at evaporation regime. For PII-2T and DPP-BTz, the films printed in evaporation regime show clear twinned morpology.

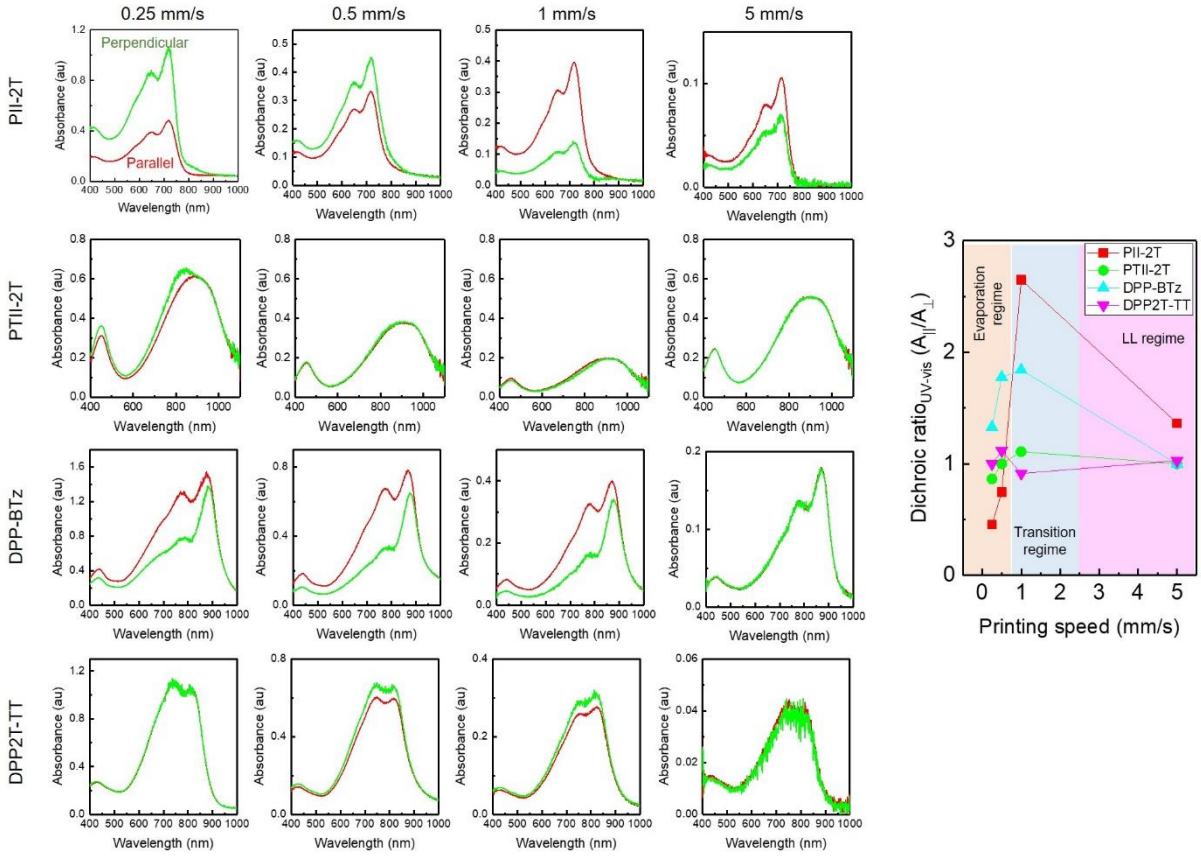


**Fig. S35. Characterization of the polymer film alignment.** Polarized absorption spectra of PII-2T, PTII-2T, DPP-BTz and DPP2T-TT films are shown with the light polarization direction oriented either parallel (red line) or perpendicular (green line) to the printing direction. The degree of alignment of the polymer backbone was characterized using the dichroic ratio $R = A_{||}/A_{\perp}$, with the peak absorbance obtained at ~420 nm. The printing speed-dependent dichroic ratio shows the highest alignment in the transition regime for PII-2T and DPP-BTz, whereas the alignment is not enhanced for PTII-2T and DPP2T-TT.

## Section S9. Evidence of $N_{TB}$ mesophase in solution and in deposited thin films

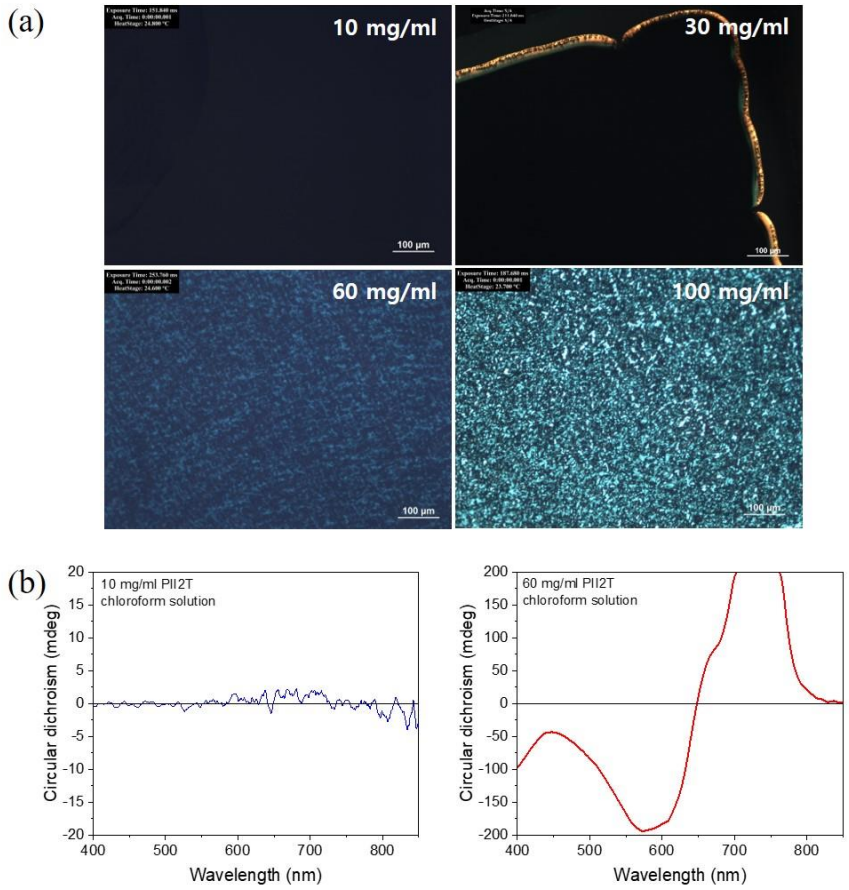


**Fig. S36. Formation of chiral, liquid crystalline mesophase in PII-2T solutions with increasing concentrations.** (a) Optical microscopic images of concentration dependent PII-2T polymer solutions. Each 2 μL polymer solutions sandwiched between two glass slides are imaged under crossed polarizers. Highly concentrated PII-2T solutions (60 and 100 mg/ml) exhibit strong birefringence over a large area. The relatively low PII-2T solutions (10 and 30 mg/ml) produce birefringence only around the solution edge as the solvent evaporates. (b) CD spectra of 10 and 60 mg/ml PII-2T solutions. High concentrated PII-2T solution exhibit CD signals, corroborating the formation of a chiral, intermediate mesophase that can be transferred to the printed film in evaporation regime and eliminated by strong strain in transition regime.

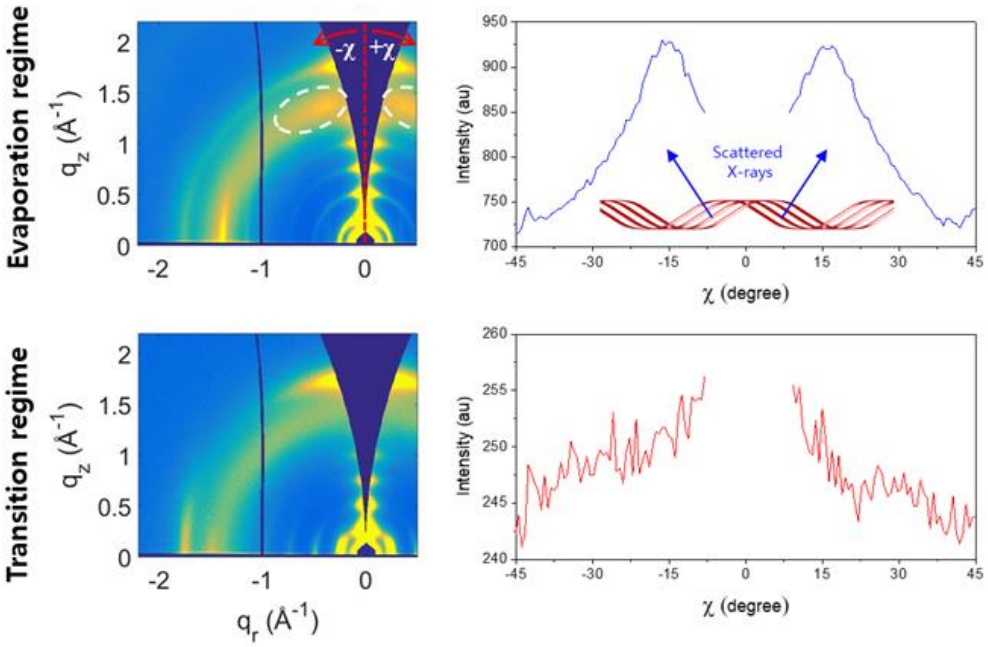


**Fig. S37. GIXD analysis of twinned morphology in PII-2T films.** The 2D X-ray scattering patterns are obtained for the PII-2T films printed in each evaporation and transition regime with the incident beam oriented parallel to the printing direction. We found that the scattering at q = ~1.42 Å$^{-1}$, which we believe corresponds to spacing derived from the liquid crystalline mesophase, is relatively more intense around $\chi = \pm 15°$ for films produced in the evaporation regime (white dashed circles in top left). We also note that these peaks are at a tilted angle and not just part of a very broad peak centered at $q_{xy} = 0$. The integrated intensity from q = 1.40 to 1.50 Å$^{-1}$ is plotted from $\chi = -45°$ to $\chi = 45°$, which clearly shows the presence of these tilted peaks (top right). We propose that these tilted peaks arise from the helical structures formed by twisted polymer chains in the evaporation regime. A schematic (inset) is drawn within the polar plot depicting how scattering from light incident on the helical structure can give rise to these tilted peaks based on the stacking within the helix. This is also supported by the fact that these tilted peaks are only seen for films printed in the evaporation regime and are absent for films printed in the transition and Landau-Levich regimes.

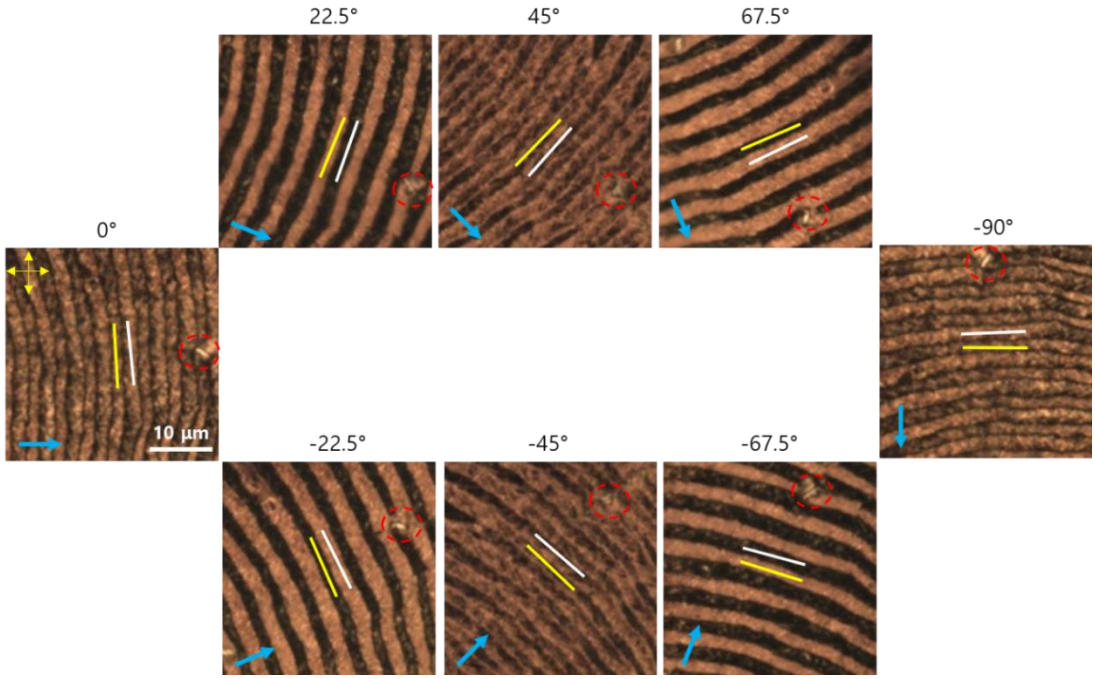


**Fig. S38. CPOM images of PII-2T twinned morphological films.** A reversing change of the alternating dark and bright band patterns is observed by rotating the sample clockwise and counter-clockwise with respect to the crossed polarizers. The blue arrow and yellow crossed arrows indicates the printing direction and the orientation of the cross-polarizers, respectively. A defect is noted by a red dashed circle which serves as a reference point to help identify the alternating birefringence of the bands (yellow and white lines).

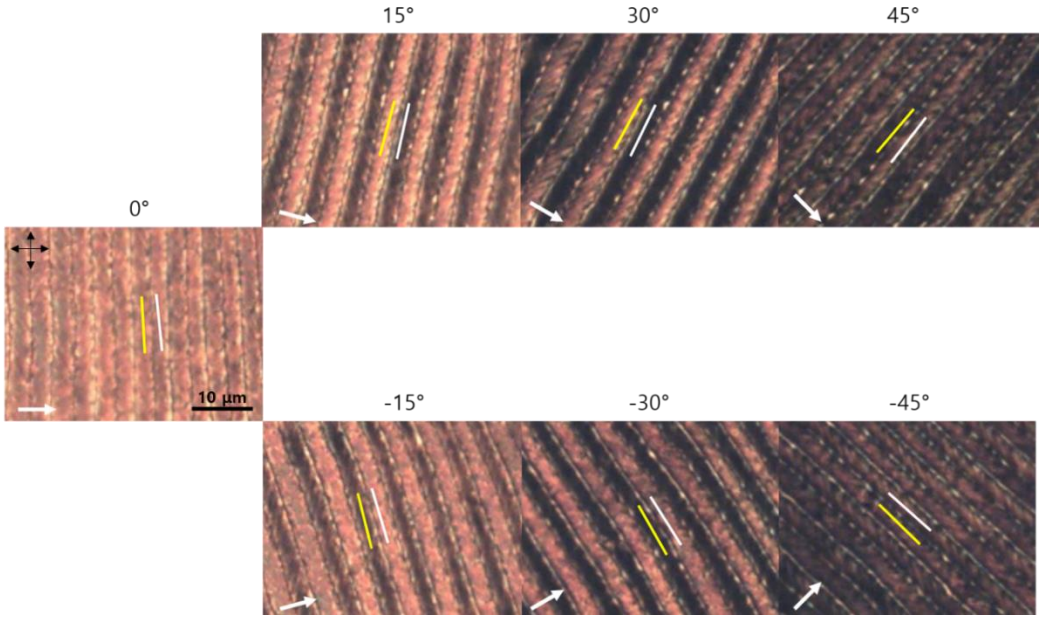


**Fig. S39. CPOM images of DPP-BTz twinned morphological films.** A similar reversing change of the alternating dark and bright band patterns is observed by rotating the sample clockwise and counter-clockwise with respect to the crossed polarizers. The white arrow and black crossed arrows indicate the printing direction and the orientation of the cross-polarizers, respectively.

To study the chirality of the twinned morphology, CD measurements were performed on the polymer films printed on glass substrates as well as polymer solutions sandwiched between two glass slides. Since some of polymer films have strong linear birefringence as we have shown with CPOM and polarized UV-Vis measurement, CD measurements were carried out with the sample rotated in-plane at 0 and 90° to rule out the birefringence phenomena (51). The CD spectra were then obtained by averaging out intensities of the measured spectra. Multiple CD measurements were performed at different positions for several samples prepared at the same condition for data reliability (fig. S40). Interestingly, only PII-2T and DPP-BTz films printed in the evaporation regime, i.e. twinned morphology films, displayed the CD signals as shown in Fig. 6E-H of the main text. Because none of the polymers we used have chiral centers in their molecular structures, we speculate that the twisted molecular conformation of polymer plays a role in developing chirality when they are assembled into the film, as in the case for PII-2T and DPP-BTz. This study also supports our hypothesis of flow-induced planarization of the polymer backbones as the CD signals are diminished with increasing printing speed.

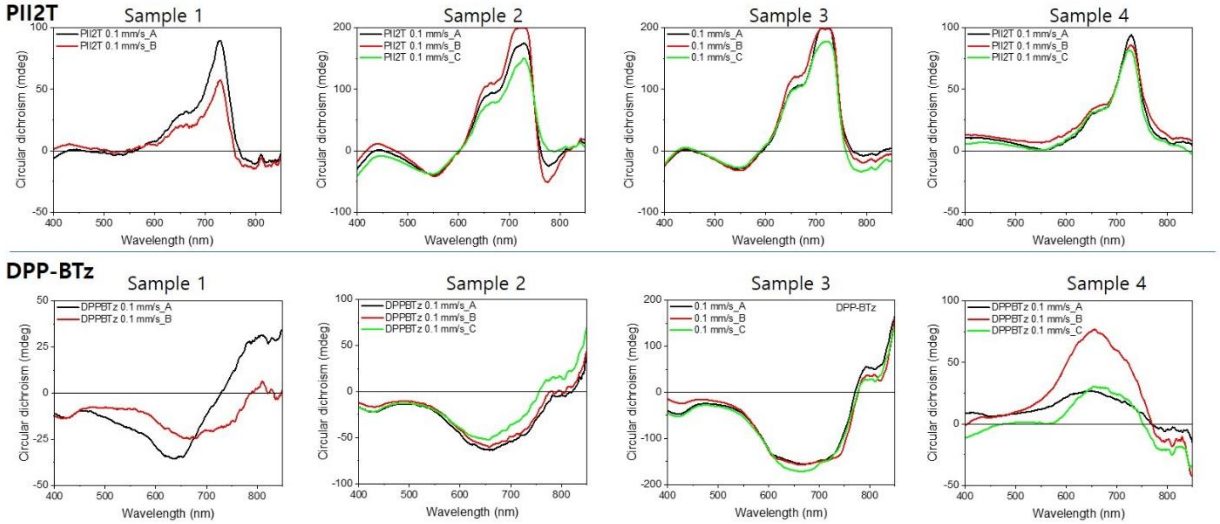


**Fig. S40. Multiple CD measurements of PII-2T and DPP-BTz films printed in evaporation regime.** The sample 1-4 denotes sample to sample measurement and the A-C denotes position to position measurements of a single sample.

**Movie S1. Solution- to solid-state phase transition of PII-2T.** Description: In-situ cross-polarized optical microscopy (CPOM) video of PII-2T assembly in a moving, drying meniscus. The meniscus was created by sandwiching the polymer solution between two glass slides. The video shows the solution phase (dark region on the left), solid thin film (brown band on the right) and the mesophase (blue band in the middle). The elliptical mesogenic domains emerge from the solution phase and coalesce to form a rope-like texture; such morphology is carried over into the solid thin film manifested as twinned domains. Figure 6A of the main text shows a representative frame of this video.

**Movie S2. Solution- to solid-state phase transition of PTII-2T.** Description: In-situ CPOM video of PTII-2T assembly in a moving, drying meniscus. In contrast to PII-2T, this material shows no mesophase near the triple phase contact line. Figure 6B of the main text shows a frame from this video.

**Movie S3. Solution- to solid-state phase transition of DPP-BTz.** Description: In-situ CPOM videos of DPP-BTz assembly in a moving, drying meniscus, showing a similar phenomenon as PII-2T. Figure 6C of the main text shows a frame from this video.

**Movie S4. Solution- to solid-state phase transition of DPP2T-TT.** Description: In-situ CPOM videos of DPP2T-TT assembly in a moving, drying meniscus, showing a similar phenomenon as PTII-2T. Figure 6d of the main text shows a frame from this video.